

©2014

Vipul Baxi

ALL RIGHTS RESERVED

**WIDE-FIELD MODULATED IMAGING FOR NON-
INVASIVE QUANTIFICATION OF TISSUE PROPERTIES:
A METHOD DEVELOPMENT STUDY**

By

VIPUL ATULKUMAR BAXI

A thesis submitted to the

Graduate School-New Brunswick

Rutgers, The State University of New Jersey

and

The Graduate School of Biomedical Sciences

University of Medicine and Dentistry of New Jersey

in partial fulfillment of the requirements

for the degree of

Master of Science

Graduate Program in Biomedical Engineering

Written under the direction of

Mark C. Pierce, PhD

and approved by

New Brunswick, New Jersey

January, 2014

ABSTRACT OF THE THESIS

WIDE-FIELD MODULATED IMAGING FOR NON-INVASIVE QUANTIFICATION OF TISSUE PROPERTIES: A METHOD DEVELOPMENT STUDY

By
VIPUL ATULKUMAR BAXI

Thesis Director:
Mark C. Pierce, PhD

Modulated Imaging (MI) is a recently reported method for rapid, non-invasive quantification of tissue optical properties (reduced scattering, μ'_s and absorption, μ_a), which can be performed across a range of optical wavelengths to determine chromophore concentrations. In this thesis, development and characterization of a compact, low cost MI system is reported, using off-the-shelf hardware components with a custom software interface capable of easy modification for specific applications. This prototype setup consists of a color CCD camera which captures the diffusely reflected light from an object illuminated with patterns generated by a miniature projector. Broadband white light from the projector is delivered through a filter wheel containing narrowband filters for measurement at 420nm, 570nm, and 620nm wavelengths. A software application in MATLAB was written to control and synchronize the phase-shifted illumination patterns with image acquisition, and perform processing of image data into optical property maps. System accuracy was characterized by measuring a series of tissue simulating phantoms fabricated with varying μ'_s and μ_a , with both the prototype platform and a commercially available MI system as a reference. The overall error of the prototype system, for μ'_s ranging from 0.93-2.23mm⁻¹ and μ_a ranging from 0.009-0.049mm⁻¹, was approximately

10% and 16%, respectively. Utilizing a lookup table that requires measurements at two illumination spatial frequencies instead of performing a least-squares fit to diffuse reflectance measurements at ten frequencies reduced the acquisition and processing time by 80%, while reducing the accuracy of optical property determination by approximately 3%.

In summary, a prototype MI platform was developed and shown to be capable of quantifying the optical properties within biologically relevant μ'_s and μ_a ranges. The system was assembled for less than 10% of the cost of commercially available systems while enabling individual components to be upgraded for a wider range of accurate optical property determination. Scattering and absorption maps obtained at multiple wavelengths can subsequently be used to quantify the concentrations of various tissue chromophores including hemoglobin, water, and lipids. Non-invasive, image based acquisition of such information may have impact in medical applications, ultimately improving patient health through disease characterization and monitoring progress of treatment.

ACKNOWLEDGEMENTS

There are several people who have played a major role in supporting my pursuit of a Master's degree in Biomedical Engineering. Firstly, I want thank Dr. Pierce for his guidance and support throughout this entire process. He has been an amazing advisor and mentor, and has put in a lot of effort to help me reach this milestone. I also want to give a special thanks to Ligin Solamen, summer program student (RISE at Rutgers) from Loyola University, who was very helpful in helping with creating phantoms for testing and characterization of the system. A special thank you to Dr. Berthiaume and Dr. Boustany for willing to be part of this thesis and helping me reach my goal.

I also want to give a big thanks to Dr. Roblyer and his staff at Boston University for assisting with the software development of the system and allowing us to use their commercial instrument as a reference system to validate our setup.

Thank you to my team at Omnyx (GE Healthcare) for being supportive and understanding while I pursued this degree. They have been extremely flexible every time I had to leave in the middle of the work day for classes, conferences, or to work on this thesis.

Last, but not the least, I want to thank my family and friends for always motivating me and reminding me that this is all worth it. Without their support, this would have not been a reality.

DEDICATIONS

This Thesis is dedicated to:

My Mom and Dad – who have always supported and motivated me

and

My Wife – the source of my inspiration!

TABLE OF CONTENTS

ABSTRACT OF THE THESIS.....	ii
ACKNOWLEDGEMENTS.....	iv
DEDICATIONS	v
LIST OF FIGURES.....	vii
LIST OF TABLES.....	ix
CHAPTER 1: INTRODUCTION	1
1.1 MOTIVATION AND SIGNIFICANCE	1
1.2 MODULATED IMAGING (MI) PRINCIPLES.....	4
1.3 CURRENT CLINICAL APPLICATIONS.....	11
1.4 PROJECT SCOPE.....	12
CHAPTER 2: MODULATED IMAGING SETUP.....	14
2.1 HARDWARE.....	14
2.2 SOFTWARE.....	21
2.3 STRUCTURED LIGHT PROJECTION.....	27
CHAPTER 3: PHANTOM FABRICATION	29
3.1 FABRICATION PROCEDURE.....	29
3.2 EFFECTS OF TITANIUM DIOXIDE & NIGROSIN.....	32
3.3 PHANTOMS FOR SYSTEM ACCURACY TESTING.....	35
CHAPTER 4: SYSTEM PRECISION & ACCURACY.....	38
4.1 SYSTEM CHARACTERIZATION	38
4.2 VARYING PHANTOMS EXPERIMENT	41
4.3 2-FREQUENCY LUT - METHOD EVALUATION.....	55
4.4 ABSORPTION SPECTRUM PREDICTION	59
CHAPTER 5: DISCUSSION	62
5.1 DISCUSSION OF RESULTS.....	62
5.2 PROPOSED FUTURE WORK.....	67
5.3 SUMMARY AND CONCLUSION	69
CHAPTER 6: REFERENCES.....	71

LIST OF FIGURES

FIGURE 1: MODULATED IMAGING OF A REFERENCE PHANTOM AT SPATIAL FREQUENCY F REQUIRES COLLECTION OF THREE SEPARATE IMAGES, CORRESPONDING TO THE MODULATED ILLUMINATION PATTERN AT THREE PHASE-SHIFTED POSITIONS. THESE THREE IMAGES ARE COMBINED USING EQ. 2 TO GENERATE A SINGLE DEMODULATED IMAGE M_{AC} , WHICH INCORPORATES THE SAMPLE DIFFUSE REFLECTANCE AT F , AND ANY SYSTEM RESPONSE FACTORS.	6
FIGURE 2: MODULATED IMAGING OF AN UNKNOWN SAMPLE	7
FIGURE 3: SCHEMATIC ILLUSTRATION OF MEASURED DIFFUSE REFLECTANCE (R_D) VERSUS ILLUMINATING SPATIAL FREQUENCY (F) AT ILLUMINATION WAVELENGTH λ_1	8
FIGURE 4: LEAST SQUARES FIT OF A MODEL FUNCTION TO MEASURED R_D VALUES, ALLOWING ESTIMATION OF OPTICAL PROPERTIES (μ_A AND μ'_s)	9
FIGURE 5: LOOK-UP TABLE METHOD FOR OBTAINING OPTICAL PROPERTIES FROM R_D VALUES MEASURED AT ONLY TWO SPECIFIC SPATIAL FREQUENCIES (F_1 AND F_2). THE FORWARD MODEL IS USED TO CREATE A MAP OF PREDICTED R_D VALUES FOR GIVEN μ_A AND μ'_s COMBINATIONS AT (F_1 AND F_2). MEASURED R_D VALUES ARE THEN MAPPED TO A SPECIFIC POINT IN THE 2-D SPACE WHICH CAN BE INTERPOLATED TO μ_A AND μ'_s VALUES.	10
FIGURE 6: PROTOTYPE MODULATED IMAGING (MI) SETUP. (A) CAMERA, (B) PROJECTOR, (C) BANDPASS FILTERS, (D) LINEAR POLARIZERS, (E) COMPUTER.	14
FIGURE 7: METHODOLOGY FOR SELECTING AN APPROPRIATE CAMERA LENS	16
FIGURE 8: SPECTRAL RESPONSE OF THE TI PICO PROJECTOR'S WHITE LIGHT EMISSION SPECTRUM (BLACK, LEFT Y-AXIS), OVERLAID WITH THE TRANSMISSION CHARACTERISTICS OF THE SELECTED BANDPASS FILTERS (RED, GREEN, BLUE, RIGHT Y-AXIS).	18
FIGURE 9: MI SYSTEM FILTER WHEEL WITH 470NM, 520NM, AND 620NM NARROWBAND FILTERS INSTALLED	19
FIGURE 10: LIGHT-TIGHT CASING AROUND THE PROTOTYPE MI SYSTEM	20
FIGURE 11: EFFECT OF CROSSED LINEAR POLARIZERS AND LIGHT-TIGHT CASING ON IMAGE QUALITY	20
FIGURE 12: SCREENSHOT OF THE CUSTOM GRAPHICAL USER INTERFACE (GUI) FOR PROTOTYPE MI SYSTEM	22
FIGURE 13: ABSORPTION AND SCATTERING SPECTRA OF THE CALIBRATION PHANTOM, INDEPENDENTLY MEASURED USING FDPM	24
FIGURE 14: MATLAB BASED MI SOFTWARE OUTPUT DURING IMAGING OF AN UNKNOWN SAMPLE	27
FIGURE 15: CHARACTERIZATION OF STRUCTURED LIGHT PROJECTION: CONVERSION BETWEEN DIGITAL PROJECTION OF STRUCTURED PATTERN TO ACTUAL LINE PAIR WIDTH (LP/MM).	28
FIGURE 16: PHANTOMS WITH VARYING NIGROSIN (TOP) AND VARYING TiO_2 (BOTTOM) CONTENT	29

FIGURE 17: PLOT OF PHANTOM NIGROSIN CONTENT VS. MEASURED SCATTERING COEFFICIENT (REFERENCE LAB)	34
FIGURE 18: PLOT OF PHANTOM TiO_2 CONTENT VS. MEASURED ABSORPTION COEFFICIENT (REFERENCE LAB)	34
FIGURE 19: PROTOTYPE MI SYSTEM SENSITIVITY: GRAYSCALE DIGITAL PROJECTION LEVEL VS IMAGE CAPTURED LEVEL	39
FIGURE 20: PRECISION & REPRODUCIBILITY MEASUREMENT LOCATIONS	39
FIGURE 21: R_D MEASUREMENTS AT THE SAME AND DIFFERENT LOCATIONS ON A HOMOGENEOUS PHANTOM	40
FIGURE 22: VARYING ABSORPTION / FIXED SCATTERING PHANTOMS: OPTICAL PROPERTIES VS. NIGROSIN CONTENT FOR REFERENCE AND TEST SYSTEMS	43
FIGURE 23: VARYING ABSORPTION / FIXED SCATTERING PHANTOMS: RELATIONSHIPS BETWEEN REFERENCE AND TEST SYSTEMS FOR μ_A AND μ'_S CALCULATIONS.	44
FIGURE 24: VARYING SCATTERING / FIXED ABSORPTION PHANTOMS: OPTICAL PROPERTIES VS. TiO_2 CONTENT FOR REFERENCE AND TEST SYSTEMS.	47
FIGURE 25: VARYING ABSORPTION/FIXED SCATTERING PHANTOMS: RELATIONSHIPS BETWEEN REFERENCE AND TEST SYSTEMS FOR μ_A AND μ'_S CALCULATIONS.....	48
FIGURE 26: OVERALL CORRELATIONS IN PHANTOM OPTICAL PROPERTIES MEASUREMENTS BETWEEN REFERENCE AND TEST SYSTEMS (FOR ALL WAVELENGTHS COMBINED)	50
FIGURE 27: MEASURED AND THEORETICAL DIFFUSE REFLECTANCE PLOTS FOR PHANTOM SET A1-A5.	53
FIGURE 28: MEASURED AND THEORETICAL DIFFUSE REFLECTANCE PLOTS FOR PHANTOM SET B1-B5.....	54
FIGURE 29: DIFFUSE REFLECTANCE (R_D) VS. SPATIAL FREQUENCY FOR PHANTOM SET “A” (TOP) AND PHANTOM SET “B” (BOTTOM)	57
FIGURE 30: RELATIONSHIPS BETWEEN OPTICAL PROPERTY MEASUREMENTS GENERATED BY LEAST-SQUARES FITTING (FIT) AND LOOKUP TABLE (LUT) METHODS.....	58
FIGURE 31: EXAMPLE OF OPTICAL PROPERTY MAPPING OF A PHANTOM COMPOSITE: FOUR PHANTOMS WITH DIFFERENT ABSORPTION AND SCATTERING PROPERTIES WERE IMAGED IN A SINGLE FOV, WITH VALUES FROM THE REFERENCE MI SYSTEM OVERLAID ON EACH (TOP). OPTICAL PROPERTY MAPS WERE GENERATED USING THE LUT METHOD (BOTTOM).	59
FIGURE 32: DIFFUSE REFLECTANCE (R_D) MEASURED AT 4 WAVELENGTHS (470NM, 520NM, 620NM, 790NM) AND FIT TO AN EXPONENTIAL FUNCTION FOR SPATIAL FREQUENCIES OF 0.10 LP/MM AND 0.20 LP/MM.	61
FIGURE 33: COMPARISON BETWEEN THE ACTUAL ABSORPTION SPECTRUM MEASURED USING CONTINUOUS FDPM AND THE MI SYSTEM PREDICTION USING ONLY FOUR WAVELENGTHS WITH EXTRAPOLATION.	61
FIGURE 34: CAMERA SENSOR RESPONSE CURVES (FROM POINT GREY RESEARCH).....	66

LIST OF TABLES

TABLE 1: HIGH-LEVEL SUMMARY OF THE PRIMARY MI SYSTEM COMPONENTS	15
TABLE 2: COMPOSITION OF PHANTOMS CREATED FOR INITIAL ASSESSMENT OF CONCENTRATION EFFECTS ON OPTICAL PROPERTIES.	33
TABLE 3: COMPOSITION OF PHANTOMS DEVELOPED FOR PROTOTYPE MI SYSTEM VALIDATION; ONE SET WITH VARYING NIGROSIN (SET A), AND ANOTHER SET WITH VARYING TiO_2 (SET B).	35
TABLE 4: OPTICAL PROPERTY MEASUREMENTS FOR PHANTOMS SETS “A” AND “B” FROM THE REFERENCE LAB.	36
TABLE 5: PHANTOM SET “A”: OPTICAL PROPERTIES MEASURED ON THE PROTOTYPE MI SYSTEM USING LEAST-SQUARES FITTING TO DIFFUSE REFLECTANCE AT 10 SPATIAL FREQUENCIES.	42
TABLE 6: PHANTOM SET “B”: OPTICAL PROPERTIES MEASURED ON THE PROTOTYPE MI SYSTEM USING LEAST-SQUARES FITTING TO DIFFUSE REFLECTANCE AT 10 SPATIAL FREQUENCIES.	45
TABLE 7: OVERALL ACCURACY BETWEEN PROPOSED MI AND REFERENCE SYSTEM USING METHOD 1.....	49
TABLE 8: DIFFUSE REFLECTANCE (R_D) MEASURED AT FOUR DIFFERENT WAVELENGTHS AND TWO SPATIAL FREQUENCIES.....	60

CHAPTER 1: INTRODUCTION

1.1 MOTIVATION AND SIGNIFICANCE

Liver transplant is currently the preferred method of treatment for end-stage liver disease and acute liver failure (Sokal, Goldstein et al. 2008). However, due to a significant imbalance between the availability of suitable donor livers and the number of recipients requiring transplant results in death for majority of the patients on the waiting list (Merion, Schaubel et al. 2005) . Among the numerous reasons for an inadequate liver transplant donor pool, one major cause is the prevalence of steatotic livers in the donor population (Canelo, Braun et al. 1999). Liver steatosis, commonly known as fatty liver, is the abnormal retention of lipids within the hepatocytes and is normally associated with obesity. As of 2010, approximately one-third (1/3) of the adult US population was considered obese (BMI > 30), among which adults over the age of 60 (the age group expected to contribute a major portion to the liver donor pool) were more likely to be obese than younger adults (Ogden, Carroll et al. 2012). An increase in the acceptable donor liver pool seems unlikely due to the current upward trend of obesity in the general population; hence, alternate efforts of salvaging rejected livers for transplantation are a major area of research focus.

Liver steatosis is further categorized as either microvesicular or macrovesicular steatosis. As the name suggest, microvesicular steatosis is associated with the accumulation of relatively small lipid droplets, whereas macrovesicular steatosis involves large lipid droplets which displace the nucleus towards the cell boundary. Studies have shown steatotic liver having a survival rate of 0%, whereas fatty livers reconditioned back to healthy livers have shown survival rate close to normal 'lean' liver

transplantations (Mokuno, Berthiaume et al. 2002). The cause for 100% transplantation failure of steatotic livers is primarily attributed to their increased sensitivity to hypoxia and reoxygenation, which is reduced following the defatting process (Berthiaume, Barbe et al. 2009). Although there are ways to reduce liver steatosis through proper diet and exercise over several days, the majority of transplantation candidates are procured liver grafts that need to go through the defatting process within hours.

There is a vast amount of research being performed to improve the survival rate of liver grafts post transplantation, specifically of steatotic livers, in order to meet the high demand. *Ex vivo* machine perfusions, both hypothermic and normothermic, have shown to have significant benefits over traditional cold storage techniques, although studies with human livers have yet to be performed (Bessems, Doorschodt et al. 2007, Henry, Nachber et al. 2012). While hypothermic machine perfusion have shown improved functionality and reduced I/R injury for nonsteatotic livers (Guarrera, Henry et al. 2011), normothermic perfusion has shown superior results for macrosteatotic livers by enhancing the defatting process (Jamieson, Zilveti et al. 2011). Studies have shown that *ex vivo* normothermic perfusion for 48 and 60 hours can reduce lipid droplet size by 50% (equivalent to lean liver), while still maintaining normal liver production levels of bile, urea and albumin. Although there is potential with *ex vivo* defatting of steatotic livers, the time frame it takes to achieve this is significantly beyond the current logistics of liver transplantation, which at most should be completed within 12 hours of procurement. As machine perfusion beings to make its way into the liver transplantation market as the preferred method over cold storage, advances are being made in expediting the defatting process. One such technique is coupling the *ex vivo* normothermic perfusate medium with

effective defatting agents that would obtain the 50% reduction in lipid droplet size within just 3 hours (Nagrath, Xu et al. 2009).

For normothermic machine perfusion to become a clinical success, several challenges need to be addressed; such as portability, ability to constantly monitor liver function and suitability for transplantation (Nativ, Maguire et al. 2012). As the market moves towards the normothermic perfusion, significant research will still be required to optimize the defatting process while maintaining full organ functionality. Common challenges that occur during these research studies are (i) to determine which liver needs to go through the defatting process, (ii) to constantly monitor the ongoing defatting process, and (iii) to determine when the defatting process can be ended. As of now, the most common way of assessing hepatocyte architecture requires multiple steps; including obtaining biopsies, sending it to a histology lab for staining and evaluation by an expert pathologist. These steps add a significant portion to an extremely time sensitive process, which can likely be the difference between clinical success and failure.

To obtain widespread clinical success, a non-invasive imaging-based method to quantify lipid content would be an important component. Studies have shown that accurate quantification of the *ex vivo* absorption and scattering spectra of lipids through spectroscopy can be used to model the *in vivo* spectra and ultimately determine the lipid concentration (Pifferi, van Veen et al. 2005). Although effective, this process requires measurements to be performed in both liquid and solid phases, which may not be a suitable approach for liver transplant.

Modulated imaging (MI) has shown significant potential for non-invasively quantifying the absorption and scattering spectra of layered tissue through an imaging

technique which uses spatially modulated illumination of tissue, camera-based image acquisition, and model-based calibration and post-processing (Weber, Cuccia et al. 2009). The method has so far been demonstrated to effectively quantify tissue properties such as oxy-/deoxy-hemoglobin concentration in intact and exposed skin flaps during surgery (Mazhar, Dell et al. 2010). Current implementations of MI are still quite expensive and the technique has not yet been applied to quantify lipid content. Therefore, this thesis begins the preliminary work to address the cost and portability factor, developing a platform to enable further research on monitoring livers during the defatting process, effectively, continuously, and non-invasively.

1.2 MODULATED IMAGING (MI) PRINCIPLES

Modulated Imaging (MI) (also known as Spatial Frequency Domain Imaging (SFDI)) is a recently reported technique for quantification of tissue properties (Cuccia, Bevilacqua et al. 2005). MI acquires a sequence of images of an object using modulated (periodic / striped) illumination patterns, enabling the diffuse reflectance of the object (R_d) to be measured as a function of illuminating spatial frequency (f). The measured R_d vs. f relationship is then fit to an analytic diffuse reflectance model for $R_d(f, \mu_a, \mu'_s)$, with absorption (μ_a) and reduced scattering (μ'_s) coefficients as fitting parameters, to estimate μ_a and μ'_s coefficients of the object on a pixel-by-pixel basis. This process can be repeated at multiple wavelengths across the visible to infrared (VIS-NIR) spectrum to produce absorption ($\mu_a(\lambda)$) and scattering ($\mu'_s(\lambda)$) spectra at each spatial location in the object. Prior knowledge of individual basis spectra for pure chromophores then allows the measured $\mu_a(\lambda)$ data to be decomposed into contributions from major tissue

chromophores including oxy- and de-oxyhemoglobin, water, and lipids. The following are the steps that walk through, in detail, the image acquisition procedure and post-processing algorithm to successfully implement the MI technique (Weber, Cuccia et al. 2006, Bassi, Cuccia et al. 2008, Cuccia, Bevilacqua et al. 2009, Erickson, Mazhar et al. 2010).

Step 1: Use a forward model (Eq. 1) based on the analytical diffusion equation or Monte Carlo simulation to predict the diffuse reflectance of an object (R_d) as a function of the illuminating spatial frequency (f), and the absorption (μ_a) and reduced scattering (μ'_s) coefficients of the object:

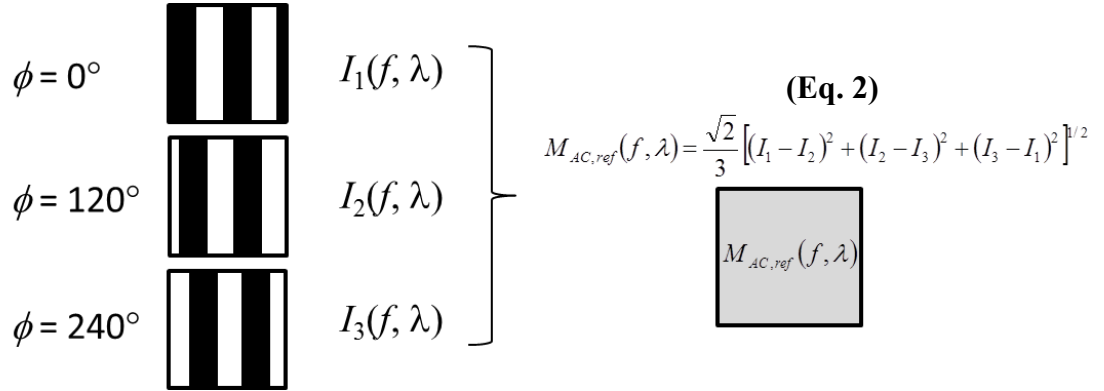
$$R_d(f, \mu_a, \mu'_s) = \frac{3Aa'}{(\mu'_{eff}/\mu_v + 1)(\mu'_{eff}/\mu_v + 3A)} \quad (\text{Eq. 1})$$

Step 2: Obtain a homogenous tissue simulating phantom (containing a combination of absorption and scattering elements) with *known* absorption $\mu_a(\lambda)$ and scattering $\mu'_s(\lambda)$ spectra covering the wavelength range of interest (~400 nm–800 nm). These reference spectra can be obtained by performing an independent frequency-domain photon migration (FDPM) measurement of the phantom.

(The following steps are performed for each specific wavelength.)

Step 3: Using the reference $\mu_a(\lambda)$ and $\mu'_s(\lambda)$ spectra for the phantom from *Step 2*, extract the absorption and scattering coefficients at the desired wavelength(s) at which MI will be performed. Use these coefficients in the forward model from *Step 1* to generate *predictions* for the diffuse reflectance ($R_{d,pred}$) at each of several illuminating spatial frequencies (f).

Step 4: Image the reference phantom from *Step 2* at the same spatial frequencies used to generate $R_{d,pred}$ values from the model in *Step 3* (Figure 1), using each of the desired illumination wavelengths in turn. At each wavelength (λ), for each spatial frequency (f), three separate images are acquired by projecting the pattern onto the sample with three lateral phase shifts (0° , 120° , and 240°). These three images are combined using Eq. 2 to obtain a single demodulated image, termed $M_{AC,ref}(f, \lambda)$, for each spatial frequency and wavelength.



The diagram illustrates the process of combining three phase-shifted images. On the left, three vertical bars represent the modulated illumination patterns for phase shifts $\phi = 0^\circ$, $\phi = 120^\circ$, and $\phi = 240^\circ$. Each bar is labeled with its corresponding intensity function: $I_1(f, \lambda)$, $I_2(f, \lambda)$, and $I_3(f, \lambda)$. A large right-facing curly bracket groups these three functions. To the right of the bracket, the equation (Eq. 2) is shown:
$$M_{AC,ref}(f, \lambda) = \frac{\sqrt{2}}{3} \left[(I_1 - I_2)^2 + (I_2 - I_3)^2 + (I_3 - I_1)^2 \right]^{1/2}$$
 Below the equation, a gray square box contains the label $M_{AC,ref}(f, \lambda)$, representing the final demodulated image.

Figure 1: Modulated imaging of a reference phantom at spatial frequency f requires collection of three separate images, corresponding to the modulated illumination pattern at three phase-shifted positions. These three images are combined using Eq. 2 to generate a single demodulated image M_{AC} , which incorporates the sample diffuse reflectance at f , and any system response factors.

Step 5: Note that the $M_{AC,ref}(f, \lambda)$ images acquired in *Step 4* are not equal to the object's diffuse reflectance $R_d(f, \lambda)$ at this stage. This is because the measured $M_{AC,ref}(f, \lambda)$ images result from the combination of sample $R_d(f, \lambda)$ with system response factors due to individual illumination and imaging components and their configurations. An instrument *correction factor* can be calculated for each spatial frequency and wavelength by dividing

each measured $M_{AC,ref}(f, \lambda)$ by the corresponding *theoretical* diffuse reflectance of the reference phantom ($R_{d,ref,pred}$), obtained in *Step 3* (Eq. 3). This correction factor is unique to the wavelength being used in this particular MI setup only. Different MI systems and wavelengths will have their own unique correction factors.

$$\text{Correction Factor} = \frac{M_{AC,ref}(f, \lambda)}{R_{d,ref,pred}(f, \lambda)} \quad (\text{Eq. 3})$$

Step 6: Image the object of interest (with unknown optical properties) using the same structured illumination method as used for the reference phantom described in *Step 4*, and shown in Figure 2. As in *Step 4*, combine the three phase shifted images obtained at each frequency using Eq. 4, to obtain the demodulated $M_{AC}(f, \lambda)$ for the unknown sample.

$$\begin{array}{ccc}
 \phi = 0^\circ & \begin{array}{|c|} \hline \text{Image 1} \\ \hline \end{array} & I_1(f, \lambda) \\
 \phi = 120^\circ & \begin{array}{|c|} \hline \text{Image 2} \\ \hline \end{array} & I_2(f, \lambda) \\
 \phi = 240^\circ & \begin{array}{|c|} \hline \text{Image 3} \\ \hline \end{array} & I_3(f, \lambda)
 \end{array}
 \left. \vphantom{\begin{array}{c} I_1 \\ I_2 \\ I_3 \end{array}} \right\} \quad (\text{Eq. 4})$$

$$M_{AC}(f, \lambda) = \frac{\sqrt{2}}{3} \left[(I_1 - I_2)^2 + (I_2 - I_3)^2 + (I_3 - I_1)^2 \right]^{1/2}$$

$M_{AC}(f, \lambda)$

Figure 2: Modulated imaging of an unknown sample

Step 7: Obtain the actual diffuse reflectance of the sample of interest $R_d(f, \lambda)$, by dividing the measured $M_{AC}(f, \lambda)$ at each frequency by the previously calculated correction factor (Eq. 5).

$$R_d(f, \lambda) = \frac{M_{AC}(f, \lambda)}{\text{CorrectionFactor}(f, \lambda)} \quad (\text{Eq. 5})$$

This process generates diffuse reflectance (R_d) values as a function of illuminating spatial frequency (f) for the object of interest at a specific wavelength (λ), which can be plotted as shown in Figure 3. Due to the low-pass characteristic of biological tissue, as the illuminating spatial frequency increases (f_1 to f_5), the measured diffuse reflectance $R_d(f)$ decreases monotonically.

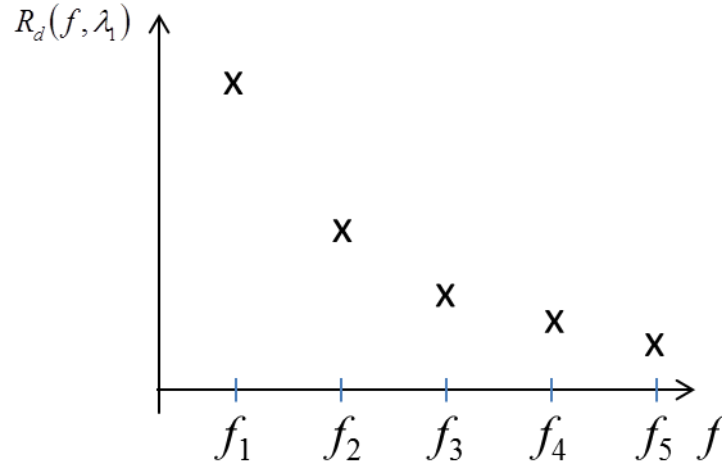


Figure 3: Schematic illustration of measured diffuse reflectance (R_d) versus illuminating spatial frequency (f) at illumination wavelength λ_1

Step 8: Given data of the form illustrated schematically in Figure 3, there are two methods that can be employed to extract the absorption and scattering coefficients from the R_d versus f profile:

Method 1: The experimentally measured diffuse reflectance values can be fit using a least-squares method, to the diffuse reflectance model from *Step 1* with absorption and scattering coefficients as fitting parameters (Figure 4). Since this method performs a least-squares fit of R_d values at up to 10 spatial frequencies, it is expected to be highly accurate, but will be computationally intensive when performed at each pixel in an entire field-of-view (FOV). This fitting method can be used when imaging homogenous phantoms where the measured R_d values can be averaged across multiple pixels and then fit to obtain single optical property values within a region of interest, or entire field-of-view.

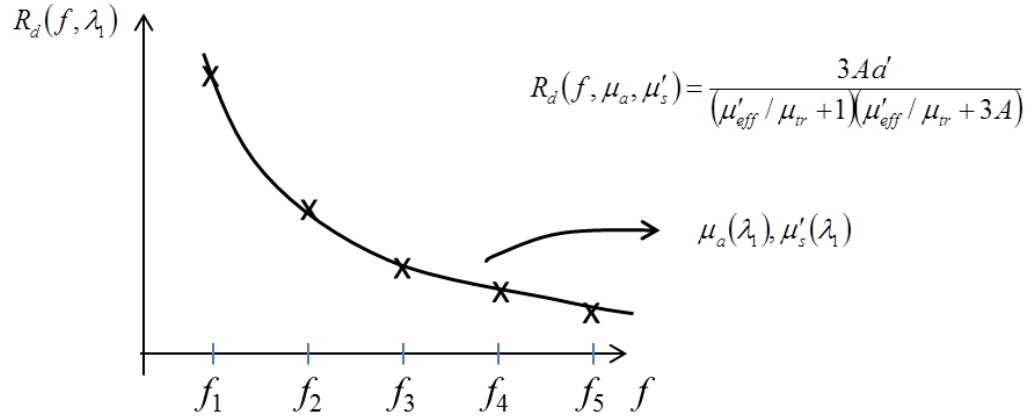


Figure 4: Least squares fit of a model function to measured R_d values, allowing estimation of optical properties (μ_a and μ'_s)

Method 2: This method for extracting μ_a and μ'_s from $R_d(f)$ measurements requires only two appropriately chosen spatial frequencies to estimate the object's optical properties, instead of up to 10 frequencies required for the model fitting approach. Two unique spatial frequencies (f_1 and f_2) are chosen and a look-up table (LUT) of corresponding diffuse reflectance values is generated by using a forward model (Eq. 1) with a range of

absorption and scattering coefficients. Any subsequently measured pair of diffuse reflectance values $R_d(f_1)$ and $R_d(f_2)$ can be mapped to a unique pair of μ_a and μ'_s via the generated LUT, as depicted in Figure 5. Since this method employs a pre-calculated LUT, this method is preferred when imaging a heterogeneous sample where μ_a and μ'_s are to be determined at each pixel across an extended field-of-view.

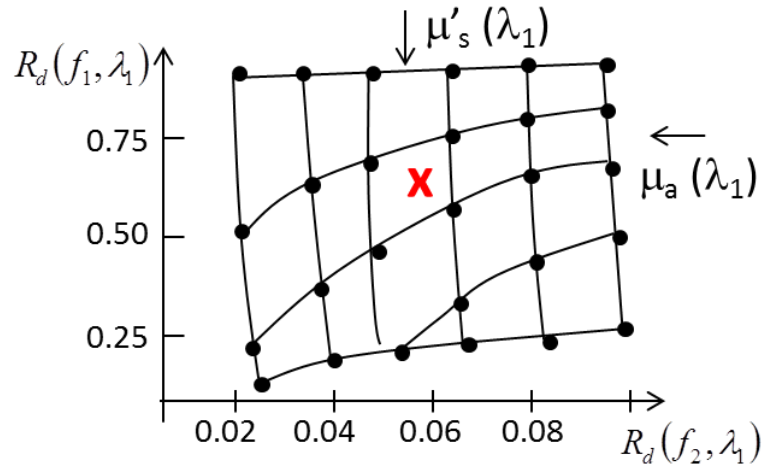


Figure 5: Look-up table method for obtaining optical properties from R_d values measured at only two specific spatial frequencies (f_1 and f_2). The forward model is used to create a map of predicted R_d values for given μ_a and μ'_s combinations at (f_1 and f_2). Measured R_d values are then mapped to a specific point in the 2-D space which can be interpolated to μ_a and μ'_s values.

Steps 3 to 8 can be performed at multiple illumination wavelengths, to obtain unique absorption and scattering coefficients at each distinct wavelength. Interpolation and extrapolation of these discrete data points can be used to obtain estimates for the complete absorption and scattering spectra $\mu_a(\lambda)$ and $\mu'_s(\lambda)$. These spectra can be further decomposed into spectra of individual component chromophores, allowing quantification of concentration levels for tissue chromophores such as oxy- and de-oxyhemoglobin, water, and lipids.

1.3 CURRENT CLINICAL APPLICATIONS

Since the inception of the modulated imaging technology, it has been applied in several areas of medicine for accurate measurement of absorption and scattering spectra of various tissues. One of the initial applications tested with MI was imaging cortical absorption and scattering response during an ischemic stroke (Abookasis, Lay et al. 2009), using infrared illumination. Changes in optical properties and concentration of oxy-/deoxy-hemoglobin and total hemoglobin were measured effectively during cerebral ischemia induced in rats. Results were comparative to conventional intrinsic signal optical imaging (ISOI), with the additional advantage of obtaining unique absorption, scattering, and hemoglobin maps. *In vivo* applications have also been evaluated to measure hemoglobin parameters, although *a priori* assumptions about constant water and lipid chromophore concentrations needed to be incorporated into the model (Mazhar, Dell et al. 2010, O'Sullivan, Cerussi et al. 2012).

Other applications involving evaluating surface regions such as the skin for several medical applications have also demonstrated the clinical potential of MI. Physicians dealing with skin burns have a challenging time determining the lateral extent and depth of the burn, which factors into the preferred treatment approach and can predict overall healing time. Studies have shown the MI technique to have potential in evaluating burn depth through quantifying the extent of absorption and scattering changes in the burn region, and correlating these alterations to normal skin optical properties (Mazhar, Sharif et al. 2012). Not only can it help in characterizing the burn severity, but MI may also be a valuable tool in monitoring the progress of the treatment. Port wine stains (PWS), also known as birthmarks, have been commonly treated with pulsed dye

lasers (PDL), although objective assessment of the treatment has been lacking. MI has been shown to effectively address this issue by quantifying and monitoring levels of hemoglobin and oxygen saturation during the PWS laser treatment procedure (Mazhar, Sharif et al. 2012). Lastly, surgeries involving replacement of damaged skin tissue through transfer flaps have also been demonstrated to gain an advantage with MI. Flaps used in these injuries have had a 40%-60% failure rate post-surgery, mainly due to the inability to objectively assess tissue health during recovery. MI technology has been shown to detect changes in hemoglobin and oxygenation over a large field-of-view without requiring any surface contact (Cuccia 2012, Ponticorvo, Taydas et al. 2013). The technology has been demonstrated to be highly sensitive to changes in these hemodynamic tissue properties, potentially providing the clinician with a powerful tool to predict flap failure.

1.4 PROJECT SCOPE

The purpose of this project was to develop a cost-effective and customizable modulated imaging platform with integrated hardware and software. Currently available commercial MI systems are optimized for specific applications and allow for minimal adjustments to the imaging parameters. The goal of this thesis was to develop a similar system which incorporates the MI technique with full processing and analysis capabilities, but which allows the user to have full flexibility in component selection and modification for instrument customization and performance improvement (e.g. camera, illumination source, projection patterns, excitation wavelengths, and lookup tables are a few examples). The MI system built here uses off-the-shelf hardware components, all

synchronized and controlled via a custom software-based user-interface. The prototype system was validated against a commercially available MI system to assess accuracy, identify limitations, and highlight potential future improvements to the setup. Ultimately, the system establishes a platform which will enable researchers to extend the technology into the liver transplantation arena and play a crucial role in the evaluation and monitoring of novel liver defatting processes.

CHAPTER 2: MODULATED IMAGING SETUP

2.1 HARDWARE

The initial phase of the project was to develop a modulated imaging system from the ground up, employing the concepts described in the previous chapter. Figure 6 shows the hardware setup of the completed prototype, consisting of five (5) main components; a) camera and imaging lens, b) projector, c) filter wheel with multiple bandpass filters, d) linear polarizers, and e) a laptop computer. The imaging workflow is initiated with the laptop projecting patterned broadband white light, through a polarizer and one (1) manually selected narrowband filter, onto the object being imaged. Reflected light is imaged onto a camera, which transfers the image back to the laptop. One of the main objectives of the project was to demonstrate the ability to build an integrated MI system using relatively low-cost, off-the-shelf hardware components. (Table 1). Each component was carefully evaluated and characterized to ensure the effectiveness of the imaging system as described below.

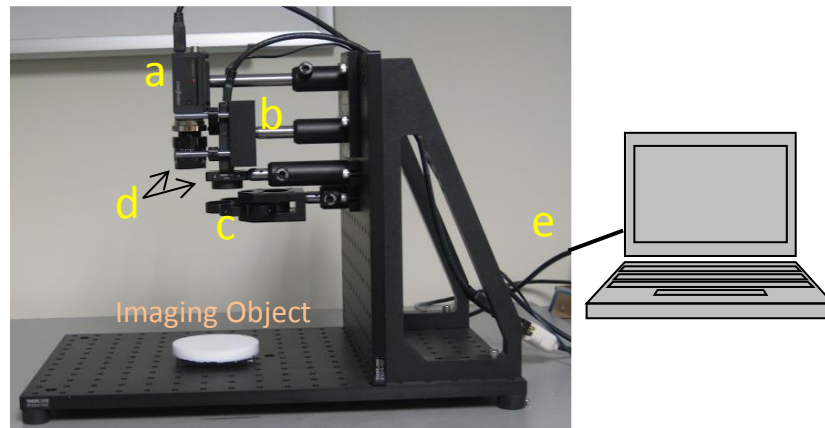


Figure 6: Prototype Modulated Imaging (MI) Setup. (a) camera, (b) projector, (c) bandpass filters, (d) linear polarizers, (e) computer.

Category	Vendor	Model	Price [\$]
Computer	Lenovo	Thinkpad T420	873
Projector	Texas Instruments	DLP Pico V2	349
Camera	Point Grey Research	Grasshopper Express, 6 MP	3995
Lens	Schneider Optics	Xenoplan 2.0/28	1375
Optics	Thorlabs	Bandpass filters	3 x 85
Optics	Thorlabs	Polarizers	2 x 89
Total			\$7,025

Table 1: High-level summary of the primary MI system components

The camera selected for the system is a Grasshopper Express® model (Point Grey Research, Canada), which consists of a six megapixel (6MP) Sony ICX694 color CCD image sensor with a $4.54\ \mu\text{m}$ pixel size. The enclosing of a type 1" image sensor (16mm diagonal) into a compact camera housing (44mm x 29mm x 58 mm) allowed the overall system to be condensed into a relatively small footprint. The camera is connected to the laptop through an IEEE-1394b interface, providing electrical power to the camera, with data transfer rates to the laptop at up to 11 frames/second (fps) at full image resolution.

To select an appropriate imaging lens for the camera, parameters defined by potential clinical applications were considered. Figure 7 shows the methodology for selecting a suitable lens, which relates the width of the CCD sensor (W_{CCD}), desired field-of-view (FOV), and working distance (WD), to the focal length of the lens, which is assumed to be approximately equal to the image distance ($u \gg v$). To achieve a FOV of 10cm at a working distance of at least 300mm with the current camera (with $W_{\text{CCD}} = 9.6\text{mm}$), the lens will require a focal length of approximately 29mm. Based on these requirements, a Schneider Optics Xenoplan compact C-mount lens (Edmund Optics, NJ)

was selected with a fixed focal length of 28mm and capability of imaging at high resolution across the visible and infrared spectrum (400-700nm).

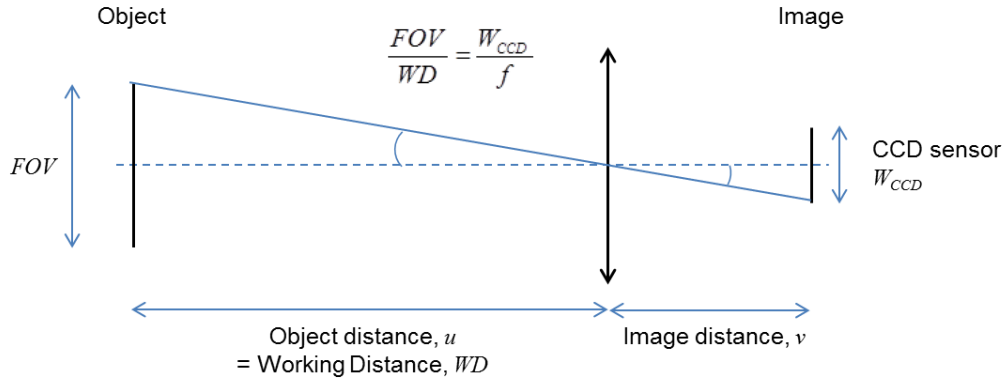


Figure 7: Methodology for selecting an appropriate camera lens

The illumination requirement for a MI system is primarily focused around projection of structured light (striped grayscale line patterns) at multiple spatial frequencies [cycles/mm] and lateral phase shifts [$^{\circ}$ or radians] onto an object plane. One method to accomplish this is by coupling a light source with a transparent Ronchi grating, printed with multiple line-pair frequencies and mounted on a motorized linear translation stage (Konecky, Mazhar et al. 2009, Chowdhury and Izatt 2013). One challenge with this approach is the synchronization of image acquisition with positioning of the motorized Ronchi grating target to ensure that the intended phase and frequency of the line pattern is accurately projected. Slight inaccuracies with the mechanics or software can lead to residual line patterns appearing in the demodulated image. A second challenge is the speed and acceleration of the translation stage, which would likely limit the overall system frame rate. A third drawback is the maximum 50% light throughput which can be achieved with a Ronchi grating. These challenges were avoided in this work by using a

digital light processor (DLP)-based projector. The unit is designed for projecting presentations onto a display screen in small conference settings, and includes an integrated red/green/blue LED light source with the inherent ability to project perfect line pair frequencies and phase shifts in the form of a digital image from a computer. This significantly simplifies the setup since no additional moving parts or components are required, while simultaneously speeding up the acquisition process through rapid image projections. For the proposed MI system, the Pico Projector Development Kit v2 (Texas Instruments, TX) was selected and connected to the computer through the HDMI port. The projector contains a digital micromirror device (DMD), which is a chip within the projector consisting of $320 \times 480 = 153,600$ individual mirrors. Each mirror is individually controlled to alternate between an on and off state, with the ratio of the on to off time allowing the projection of unique brightness levels. The DLP projector thus enabled the projection of a highly accurate and controllable sinusoidal illumination pattern, with intensity throughput increased to 68% (limited by DMD mirror reflectivity), both key criteria for MI.

Using MI to determine sample optical properties at specific optical wavelengths requires corresponding bandpass filters to be placed in the illumination pathway. To optimize selection of filters, the spectral response of the broadband “white light” emitted from the projector was measured to identify wavelengths with highest intensity for use in the prototype MI system. The projector’s illumination spectrum as shown in Figure 8 (black) was obtained using a USB2000 fiber optic spectrophotometer (Ocean Optics, FL). The LED light source in the projector is a single LED chip with separate blue, green, and red emitters, which generates strong peaks in each of these spectral regions; 460nm,

516nm, and 628nm for blue, green, and red peaks, respectively. To obtain narrowband excitation at approximately these wavelengths where the projector output intensity is greatest, bandpass filters at 470nm, 520nm, and 620nm (Thorlabs, NJ) with a full width at half-maximum (FWHM) bandwidth of approximately 10nm were integrated into the illumination path in a manual filter wheel. As shown in Figure 6, the spectral

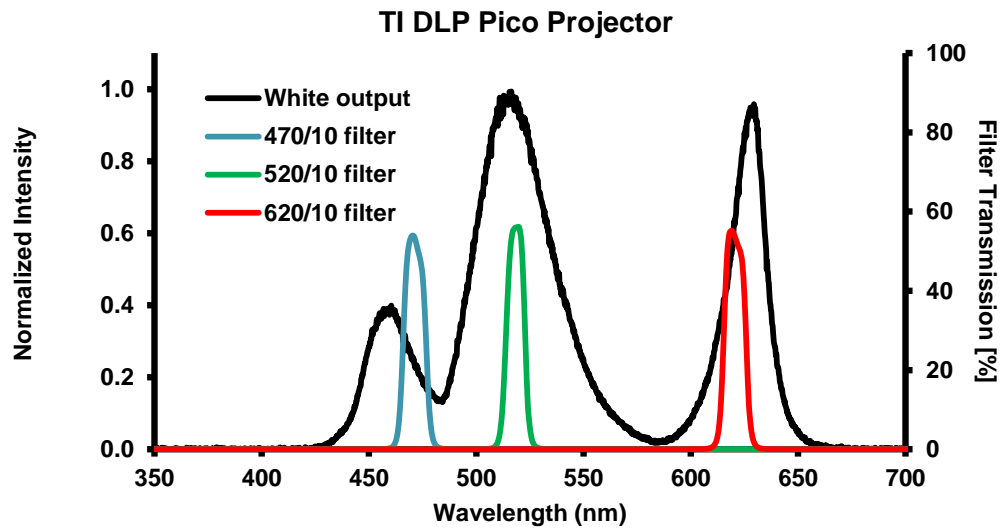


Figure 8: Spectral response of the TI Pico Projector's white light emission spectrum (black, left y-axis), overlaid with the transmission characteristics of the selected bandpass filters (red, green, blue, right y-axis).

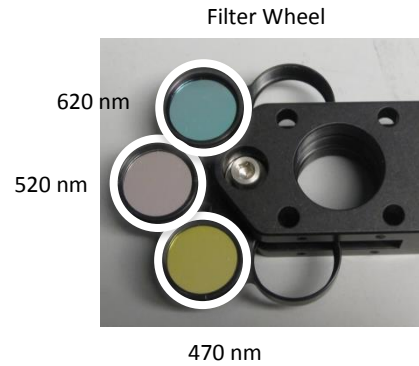


Figure 9: MI system filter wheel with 470nm, 520nm, and 620nm narrowband filters installed

response with each individual filter provided a narrowband excitation (blue, green, and red) fairly close to the optimal wavelengths. For simple implementation within the proposed system, the filters were assembled into a filter wheel, as shown in Figure 9, and mounted under the projector (Figure 6). This arrangement allowed for rapid swapping of filters without the need to disassemble and re-align components. Although not incorporated into the current design, a motorized filter wheel could be used to eliminate the need for manual switching of filters.

To eliminate bright glare from specular reflections at the sample surface, separate linear polarizers were added in front of the illumination source and the camera lens. The unpolarized light emitted from the projector is linearly polarized for illumination of the sample, with a second polarizer (in front of the camera lens) rotated until it is orientated perpendicular to the illumination polarizer, allowing only scattered (depolarized) light to



Figure 10: Light-tight casing around the prototype MI system

pass through. Further, to prevent additional ambient light from contributing to the image, a light-tight case was built around the entire setup (Figure 10), covering all slides with an opaque black cardboard. A small detachable door is built in the front to allow for easy access to the components and placement of samples for imaging. As seen in Figure 11, these minor modifications resulted in significantly improved image uniformity and quality.

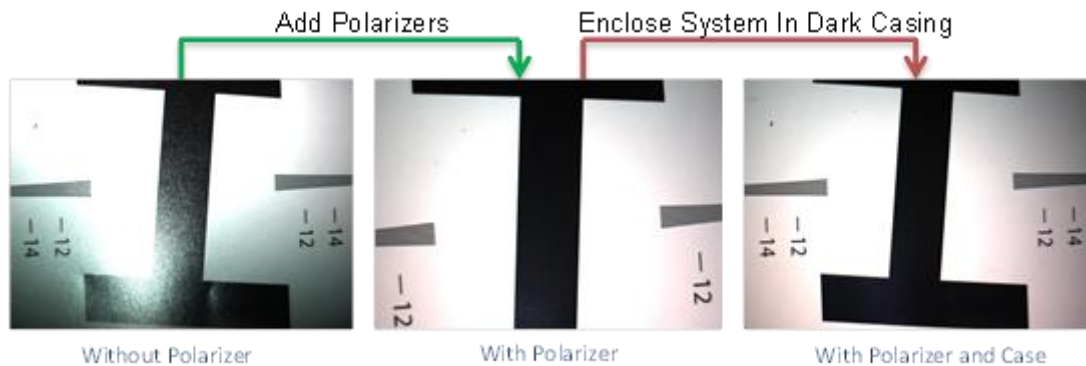


Figure 11: Effect of crossed linear polarizers and light-tight casing on image quality

The last major hardware component that integrates the entire system is the laptop computer, which runs a custom developed software application that synchronizes and controls the patterned illumination and image acquisition. The projector is connected to the laptop via the HDMI port which effectively treats the projector as an additional

display device (like a second monitor) to which digital images of sinusoidal black and white patterns are sent for projection. The camera is connected to the laptop through an IEEE-1394b Firewire 800 port, allowing the computer to trigger image acquisition synchronized with the illumination sequences, and to receive the acquired image data for post-processing. The software carrying out the imaging workflow is built on the MATLAB platform with a user interface for easy execution.

2.2 SOFTWARE

In order to customize the system with complete flexibility to vary imaging parameters, hardware components, and post-processing, a custom software application was developed in MATLAB. A front-end portion was developed using the GUIDE application in MATLAB to wrap the underlying MI algorithms into a user-friendly interface for easy implementation and operation. Within the underlying source code, MATLAB's image acquisition and image processing toolbox were utilized to control the camera and projector hardware and to perform post-processing of the image data. The software interface allows the user to easily change imaging parameters (such as line pair frequencies), to select the desired method for calculating optical properties (least-squares fitting versus lookup table), to specify the two frequencies used for the LUT, and to calibrate the system with standard phantoms.

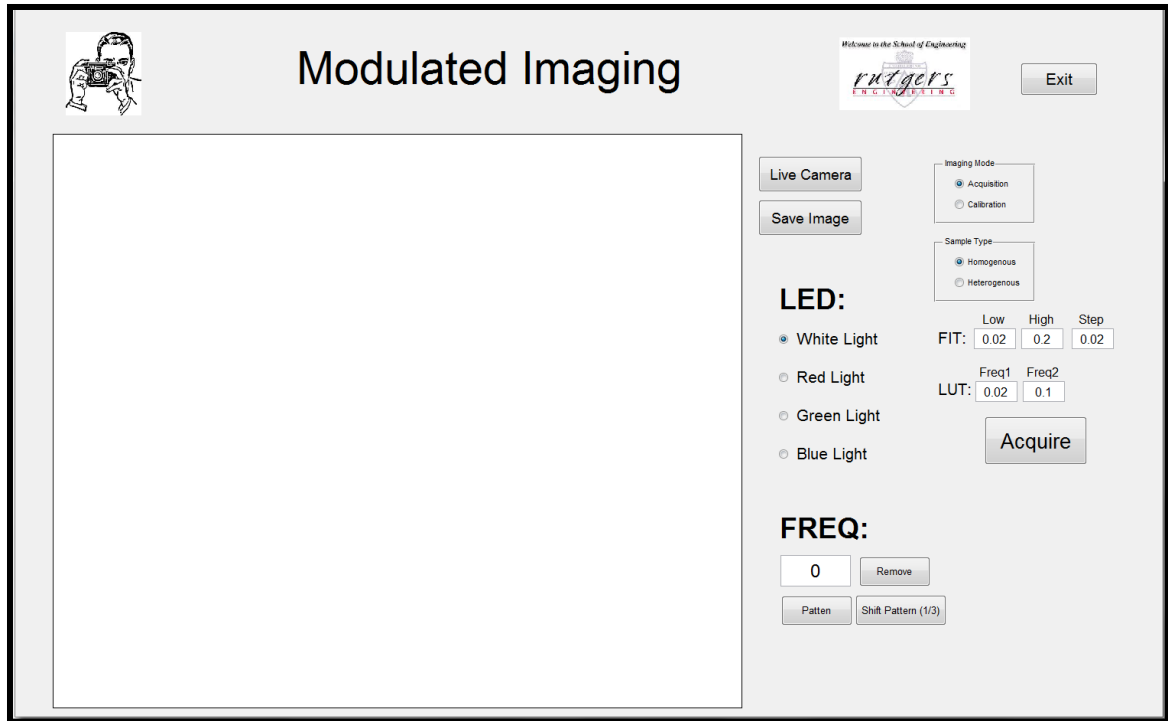


Figure 12: Screenshot of the custom Graphical User Interface (GUI) for prototype MI system

Figure 12 shows the software application interface that controls and implements the MI system. The design was developed with keeping the user friendliness and operability as a primary requirement. The main features of the software interface include controls for (a) system initiation (confirming hardware connection), (b) starting the live image viewer, (c) selection between image acquisition for initial calibration, or for imaging an unknown sample, (d) specifying the type of sample (homogenous or heterogeneous), (e) specifying frequencies for the FIT and LUT models, and (f) saving individual raw images displayed in the viewer. The current version of the software requires the MATLAB platform to be running in the background, although a stand-alone version, through C/C++ code conversion of the application has also been tested for

proper functionality. Each of the features described above was tested for accurate implementation and accuracy.

The initial step for an MI imaging session involves system calibration using a sample with known optical properties (absorption and reduced scattering coefficients across the entire spectrum). A large phantom (termed BigBoy BOT2) was obtained from a collaborating reference lab (Prof. D. Roblyer, Boston University) with 0.67g of scattering TiO_2 (Sigma-Aldrich 14027) and 3.3 mL of absorbing nigrosin (Sigma-Aldrich N4743) from a 1.5g/liter stock solution, all mixed into 2-part silicone (Ellsworth Adhesives; Corning Sylgard 184). This phantom was measured independently using an infinite-geometry, multifrequency, multidistance frequency-domain photon migration (FDPM) system at Beckman Laser Institute, (UC Irvine, CA) to precisely determine the absorption and scattering coefficients across the spectrum from 450-900nm (Figure 13). This reference phantom was placed in the prototype MI system and using the software, the calibration process was performed (Chapter 1, Steps 1-4).

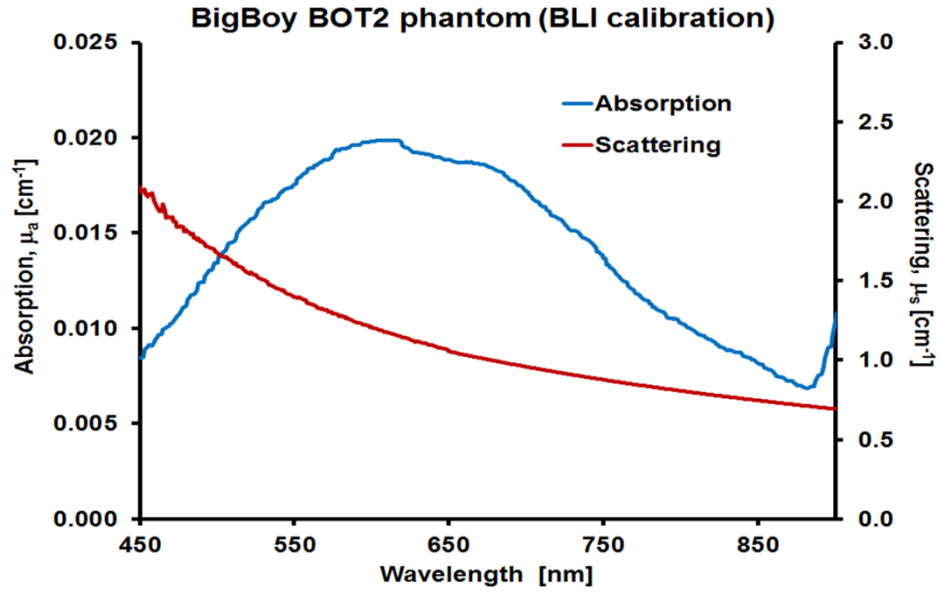


Figure 13: Absorption and scattering spectra of the calibration phantom, independently measured using FDPM

Before beginning the imaging process, the user is asked to (i) provide the location of the data file containing the FDPM-derived absorption and scattering values for the reference phantom, (ii) provide the wavelength at which the imaging is currently being performed, and (iii) provide the illumination spatial frequencies to be used for the current imaging session.

The default spatial frequencies are set to range from 0.02 mm^{-1} to 0.2 mm^{-1} with a 0.02 mm^{-1} step size (resulting in 10 total frequencies), keeping in accordance with values reported in previous publications (Cuccia, Bevilacqua et al. 2009). With this input information (items i, ii, iii above), the software begins to image the reference phantom by acquiring three phase shifted images for each spatial frequency projected onto the sample, resulting in a total of 30 raw images. The three phase shifted images at each spatial frequency are combined using the AC demodulation equation (Eq. 2) to obtain a

single M_{ac} image for each frequency. Simultaneously, the absorption and scattering coefficients for the current illumination wavelength are obtained from the reference phantom's FDPM data file. Using an analytic diffusion model, the theoretically predicted diffuse reflectance values ($R_{d,pred}(f)$) are calculated for the phantom at the user-specified frequencies used for imaging. Then, a correction factor for each frequency is obtained by forming the ratio of the experimentally measured M_{ac} to the corresponding $R_{d,pred}$ predicted by the model. These correction factors are stored within the software application folder for use with subsequent measurements on unknown objects. This set of correction factors is unique to the system conditions and setup at that moment. This calibration process is performed separately for each of the three wavelengths included in the system. Re-calibration of the system is performed anytime a change is made with the setup or parameters, such as a change in the components (i.e. camera or projector), filters, and desired illumination pattern frequencies.

Once the MI system is calibrated, it is ready for imaging of unknown samples. In a similar fashion to imaging the calibration phantom, the unknown sample is placed on the object plane, ensuring that the surface is at the same height at which the calibration was performed. Using the software interface, the "Unknown Sample" option is selected instead of "Calibration", and the illuminating spatial frequencies are input for the inverse models (either least-squares fitting "FIT" or the look-up table "LUT"). It is important to ensure that the frequencies used during imaging of an unknown sample are identical to the ones used during calibration. On selecting the "Acquire" button, the user is asked to provide the wavelength being used and then initiate the imaging of the sample, which again involves acquisition of three phase shifted images per spatial frequency projected.

The correction factor generated during calibration for each specific wavelength and spatial frequency is applied to the demodulated M_{ac} images, to ultimately obtain instrument-corrected R_d images at each spatial frequency for the unknown sample.

The final step of the MI process is then to extract the optical properties of the sample from the measured $R_d(f)$ data described above. At this stage in the MI process, we can construct an $R_d(f)$ vs f plot for each pixel in the image. The two methods employed in this system to extract μ_a and μ'_s are a least squares fit “FIT” to the full $R_d(f)$ vs f plot, or a look up table “LUT” using R_d measurements at only two specific spatial frequencies, f_1 and f_2 , previously described in Chapter 2. As described earlier, each method is used for a different purpose. Due to the extensive time required to use the FIT approach on each pixel in an image, this method is only suitable when imaging a homogenous sample, where all pixels within an entire FOV can be averaged to obtain a single R_d value for the bulk material, and the fitting process performed once. Alternatively, the LUT method is preferred when the sample is inhomogeneous and optical properties need to be calculated for each image pixel. The LUT approach may be expected to result in a slight decrease in accuracy since only two spatial frequencies are used, but the gain in speed may make this trade-off worthwhile. The MI system is currently capable of imaging homogenous objects, where the R_d values from all image pixels are averaged before processing, or to perform individual pixel processing for inhomogeneous objects. During this initial development and characterization phase, the system utilized both inverse methods (FIT and LUT) to calculate the optical properties in order to compare the accuracy of each method; the FIT method using all ten (10) $R_d(f)$ values and LUT method using only two R_d values (at f_1 and f_2). As shown in Figure 14, when the FIT method is selected, the

software plots the entire R_d values versus spatial frequency, f , and also displays the absorption and scattering coefficients calculated from both methods for comparison.

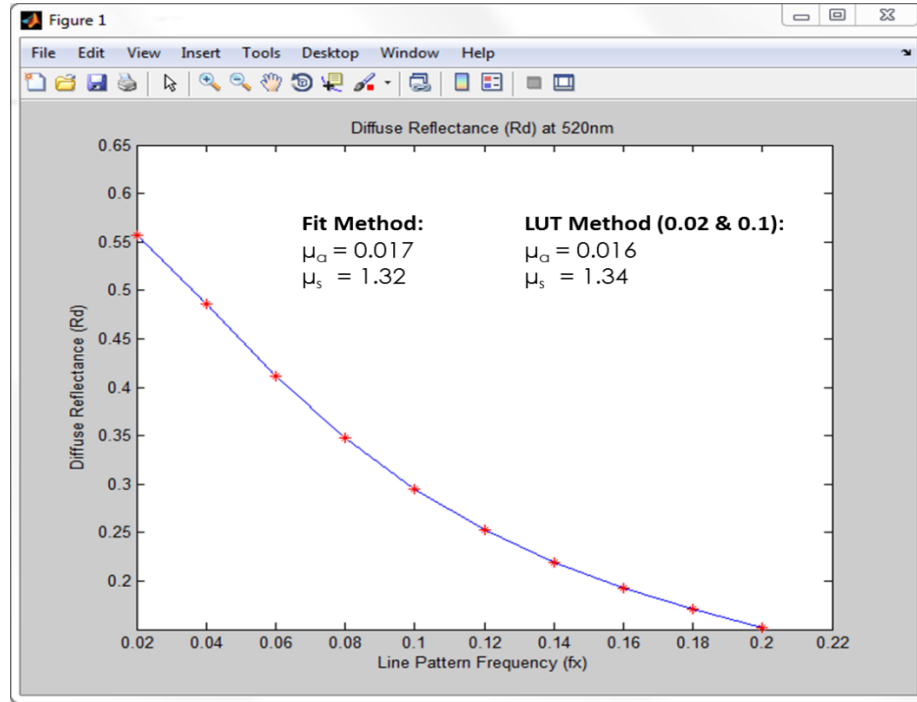


Figure 14: MATLAB based MI software output during imaging of an unknown sample

2.3 STRUCTURED LIGHT PROJECTION

One of the key requirements during initial setup of the system and software was characterization of the modulated (stripe) illumination patterns projected onto the sample. Due to the optics of the projector and camera, and the height of the sample plane, it is crucial to establish the relationship between parameters used to create the stripe patterns *in software*, to an actual number of line-pairs per mm (lp/mm) arriving *at the sample*. This relationship is important to quantify because all the mathematical models used in the MI system are based on absolute spatial frequencies in lp/mm units.

To evaluate this relationship, digital images with continuous pixel frequencies from 0-140 were created and projected onto a flat sample plane. For each frequency, the actual physical number of lp/mm being projected was measured by placing a ruler at the sample plane. This exercise was performed multiple times to ensure accuracy in the manual measurements. Figure 15 shows the relationship between the MI system parameter and the physical number of lp/mm measured, which was quantified as a linear relationship with a single conversion factor of 0.0017.

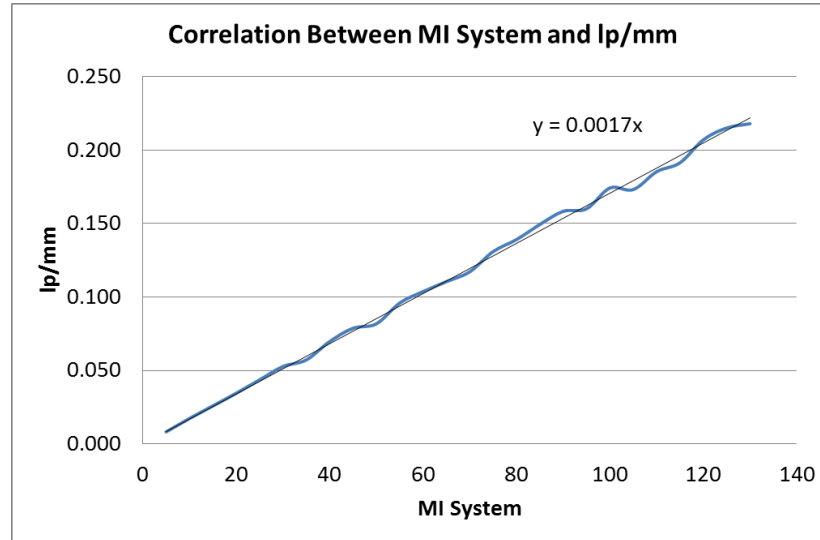


Figure 15: Characterization of structured light projection: conversion between digital projection of structured pattern to actual line pair width (lp/mm).

Therefore, when the user enters frequencies in lp/mm into the system's user-interface, the software uses this conversion factor to achieve the desired (projected) spatial frequency at the sample. This relationship is also specific to the current setup, and would need to be re-calculated if any of the components change, including their physical location in the system, or if the height of the sample plane is changed.

CHAPTER 3: PHANTOM FABRICATION

3.1 FABRICATION PROCEDURE

To characterize and validate the MI system developed here, the next step was to test the system accuracy using tissue simulating phantoms. As described in previous publications (Pogue and Patterson 2006), phantoms can be created by combining different concentrations of nigrosin (India ink) and titanium dioxide (TiO_2) in a silicone (polydimethylsiloxane, PDMS) matrix. Nigrosin, a dark ink, creates the absorption characteristic, whereas TiO_2 creates the scattering characteristic of the phantom. Varying the concentrations of these absorbing and scattering components can produce phantoms with a wide variety of optical properties. Figure 16 shows the effects of individually increasing nigrosin or TiO_2 , while keeping the other component constant. With constant TiO_2 , increasing the nigrosin concentration darkens the resulting phantom, by increasing the absorption coefficient. Alternatively, with constant nigrosin, increasing the TiO_2 concentration lightens the phantom by increasing the scattering.

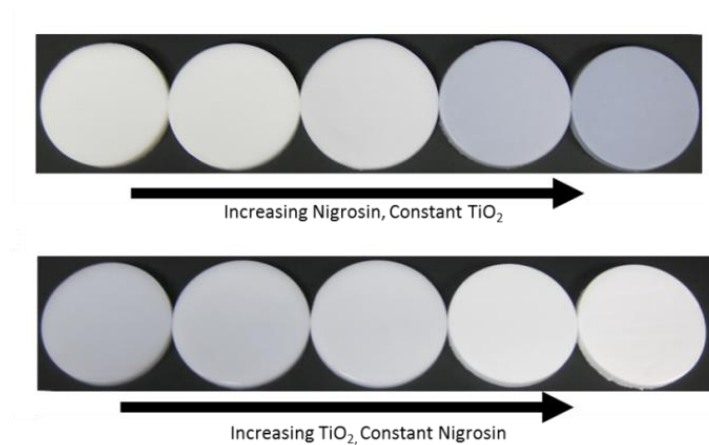


Figure 16: Phantoms with varying Nigrosin (top) and varying TiO_2 (bottom) content

The following materials are required to create tissue simulating phantoms:

- 1) Silicone base
- 2) Silicone curing agent (CA)
- 3) Absorbing agent: nigrosin (as stock solution of 0.015g nigrosin per 10ml H₂O)
- 4) Scattering agent: titanium dioxide (TiO₂)
- 5) 2x 250ml disposable plastic beakers
- 6) Petri dishes
- 7) Sand paper (fine grit)
- 8) Vacuum chamber
- 9) Mass scale
- 10) Plastic transfer pipettes
- 11) Sonicator

Follow the steps below to create phantoms with desired nigrosin and TiO₂:

- 1) In a 250 ml plastic beaker, measure out the silicone curing agent (CA) using a plastic transfer pipette (measure using the mass scale)
- 2) Tare (zero) the scale (with the beaker of 10ml of CA still on the scale) and add the desired quantity of TiO₂. Mix by swirling continuously for a few minutes.
- 3) Setup the sonicator as per its user guide and place the beaker containing the CA plus TiO₂ mix into the water. Leave the mixture sonicating for approximately 2 hours. Take the mixture out every 30 min and swirl. After 2 hours, check to ensure all TiO₂ chunks have disappeared. If not, continue sonicating until all the mixture is homogeneous.

- 4) While the sonication step is progressing, measure out the required amount of silicone base into a 250ml plastic beaker, using the mass scale.
- 5) Take the stock solution of nigrosin (0.015g/10ml of H₂O) and pipette the desired amount into the silicone base. Mix the nigrosin plus silicone base well with a spatula for 10 minutes.
- 6) After the sonication of the curing agent plus TiO₂ mixture is complete, pour the contents into the base-plus-nigrosin mixture. Mix all contents well for approximately 10 minutes.
- 7) Place the mixture into the vacuum chamber for approximately 10-20 minutes (until all the bubbles have disappeared). Be careful to avoid overflowing the container(s).
- 8) Line the bottom of the petri dishes with fine grit sand paper by taping with double sided tape.
- 9) Pour the mixture into the petri dishes. Place the petri dishes with the mixture into the vacuum chamber for additional 20-40 minutes to ensure all bubbles have disappeared.
- 10) Take the petri dishes out of the chamber and let it rest for about an hour. Any remaining bubbles should be broken with an air duster (gently)
- 11) Label the phantoms with the appropriate information (concentration of nigrosin & TiO₂ and date) and let them sit for about 2 days to allow for curing of the samples.

The phantoms created should be large enough to fill the entire FOV of the imaging system. During imaging, the side facing the bottom of the petri dish (side touching the

sand paper) should be imaged as this will prevent the side to be ‘shiny’ and highly reflective. It is also important to ensure the surface that’s being imaged is flat as possible; therefore, carefully peel the sand paper for an even surface.

3.2 EFFECTS OF TITANIUM DIOXIDE & NIGROSIN

Nigrosin, also known as India ink, is a black dye used widely in biology for negative staining of bacteria. For tissue simulating phantom fabrication, nigrosin possess a broad and smooth absorption curve across the visible wavelength spectrum (Presser 2012). Conversely, titanium dioxide is widely used as a white pigment due to its high refractive index. The opacity induced by this compound results in highly effective scattering of light in the visible spectrum (Auger, Martinez et al. 2009). These compounds are ideal for developing phantoms for testing MI systems due to their ability to accurately control absorption and scattering properties. Although both compounds are widely used in various fields of research, little data was available describing the concentrations of nigrosin and TiO_2 required to achieve phantoms with absorption and scattering coefficients in ranges which simulate biological tissue.

Therefore, before evaluating the MI system for its accuracy in quantifying sample optical properties, the nigrosin and TiO_2 compounds had to be characterized so that appropriate phantoms could be developed for the MI study. As a first pass, starting concentrations for both compounds were estimated based on the limited data available in the literature. Table 2 shows the concentrations of nigrosin and TiO_2 used.

<i>Table 2</i>	Varying Nigrosin						Varying TiO ₂				
Phantom #	1	2	3	4	5	6	1	2	3	4	5
Nigrosin [ml]	0.03	0.07	0.33	1.67	3.33	6.29	0.33	0.33	0.33	0.33	0.33
TiO ₂ [g]	0.12	0.12	0.12	0.12	0.14	0.12	0.06	0.09	0.12	0.59	1.17

Table 2: Composition of phantoms created for initial assessment of concentration effects on optical properties.

While keeping the amount of TiO₂ constant at approximately 0.12g, nigrosin was varied from 0.03ml – 6.29ml. Additionally, a separate set of phantoms were created with nigrosin held constant at 0.33ml, and TiO₂ varied from 0.06g to 1.17g. Phantom #3 was a common phantom used in both sets as it contained the midpoint concentrations for each of the varying nigrosin and TiO₂ sets.

Once fabricated, the ten phantoms were sent to a collaborating lab at (Prof. D. Roblyer, Boston University) for measurement using a commercially available MI instrument (Modulated Imaging Inc., CA). The system available at the Roblyer lab measured the absorption and scattering coefficients of each of the phantoms at ten different wavelengths ranging from 396nm to 851nm. The three wavelengths in the Roblyer lab's MI system that were closest to the prototype MI system developed here were 471nm, 526nm, and 621nm. Hence, our use of the Roblyer lab's system as a reference standard primarily focused on its measurement output at these specific wavelengths. Figures 17 and 18 show the relationships between varying amounts of nigrosin and TiO₂ used in phantom fabrication and the measured absorption and scattering coefficients, respectively, from the reference lab MI system.

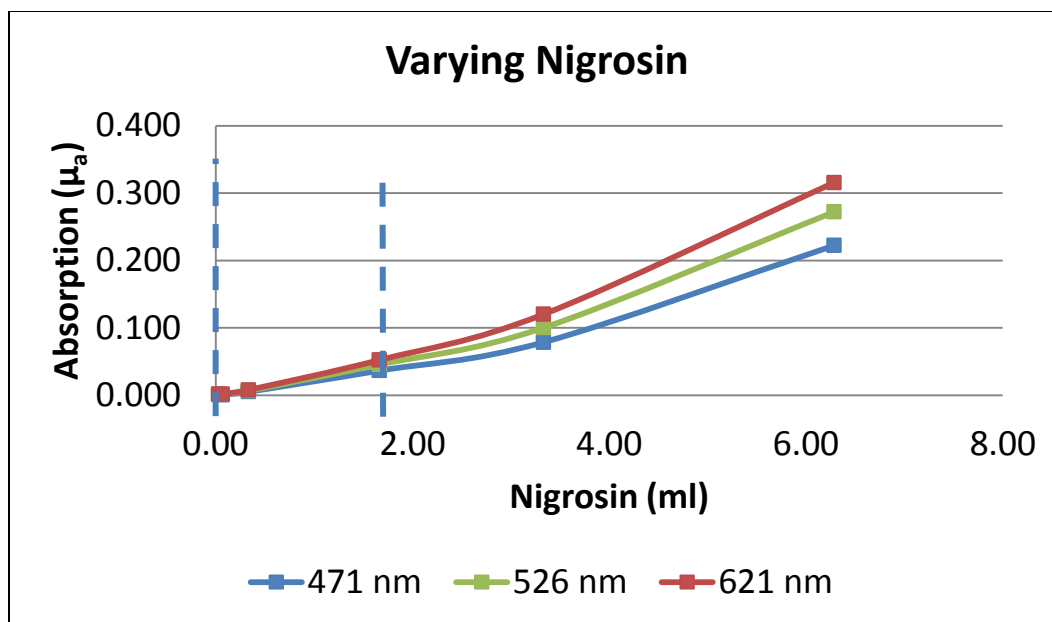


Figure 17: Plot of phantom nigrosin content vs. measured scattering coefficient (reference lab)

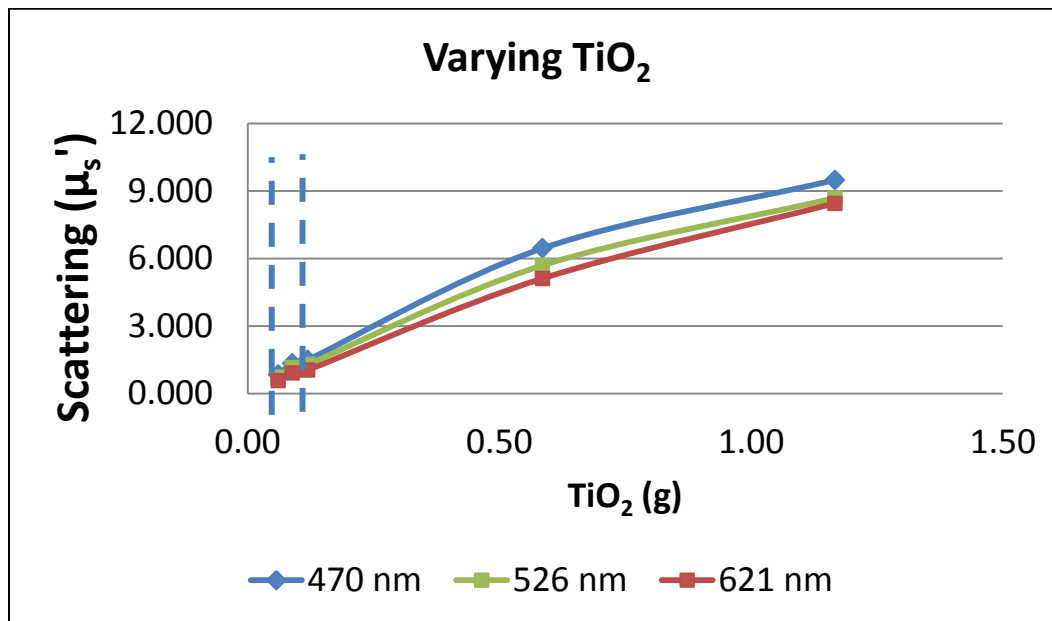


Figure 18: Plot of phantom TiO_2 content vs. measured absorption coefficient (reference lab)

Both plots, for varying nigrosin and varying TiO_2 , exhibit the expected behavior of increasing coefficient values as the concentrations of the corresponding compound increase. Evaluating the normal ranges of optical properties tested in previous studies (Cuccia, Bevilacqua et al. 2009), the absorption values range approximately between 0.001 mm^{-1} to 0.15 mm^{-1} and the scattering values range approximately between 0.5 mm^{-1} to 2 mm^{-1} . Based on the correlations established in the current study, this roughly corresponds to a nigrosin range of 0.03 ml to 1.5 ml and a TiO_2 range of 0.03 g to 0.1 g (as shown by blue dotted lines in Figure 17 and 18).

3.3 PHANTOMS FOR SYSTEM ACCURACY TESTING

Based on the findings of the previous section, a new set of phantoms was developed with modified ranges of nigrosin and TiO_2 concentration, chosen to better match the optical properties of biological tissue. Table 3 shows the concentrations of the “new” phantom sets created specifically for characterization of the MI system.

<i>Table 3</i>	Varying Nigrosin					Varying TiO_2					
Phantoms	A1	A2	A3	A4	A5	B1	B2	A3	B3	B4	B5
Nigrosin [ml]	0.03	0.08	0.25	0.63	1.66	0.25	0.25	0.25	0.25	0.25	0.25
TiO_2 [g]	0.05	0.05	0.05	0.05	0.05	0.03	0.04	0.05	0.06	0.08	0.09

Table 3: Composition of phantoms developed for prototype MI system validation; one set with varying nigrosin (Set A), and another set with varying TiO_2 (Set B).

Similar to the previous group of phantoms, two new sets were created with varying concentrations of either the nigrosin or TiO_2 , and holding the other compound

constant. Phantom #A3 was a common phantom in both sets as it had the midpoint concentration for both sets. The new phantoms were sent to the collaborating lab for reference measurements at the three wavelengths closest to those implemented in the prototype MI system.

Table 4 Reference Lab Measurements			Wavelengths [nm]					
			471		526		621	
Phantom	Nigrosin [ml]	TiO₂ [g]	μ_a	μ'_s	μ_a	μ'_s	μ_a	μ'_s
A1	0.025	0.05	0.002	1.35	0.002	1.16	0.002	0.93
A2	0.075	0.05	0.003	1.42	0.003	1.22	0.004	0.98
A3	0.250	0.05	0.011	1.40	0.013	1.21	0.015	0.97
A4	0.625	0.05	0.036	1.42	0.044	1.22	0.049	0.98
A5	1.665	0.05	0.109	1.44	0.127	1.23	0.144	0.97
B1	0.25	0.0250	0.014	0.61	0.016	0.53	0.016	0.41
B2	0.25	0.0375	0.013	0.91	0.015	0.78	0.016	0.62
A3	0.25	0.0500	0.011	1.40	0.013	1.21	0.015	0.97
B3	0.25	0.0625	0.011	1.56	0.014	1.35	0.016	1.10
B4	0.25	0.0750	0.011	1.87	0.014	1.60	0.016	1.31
B5	0.25	0.0875	0.009	2.26	0.011	1.93	0.014	1.58

Table 4: Optical property measurements for phantoms sets “A” and “B” from the reference lab

Table 4 shows absorption (μ_a) and reduced scattering (μ'_s) values measured at the collaborating lab for each of the ten phantoms (sets A and B) at wavelengths of 471 nm, 526 nm, and 621 nm. As expected from the data generated by the first phantom fabrication study, the absorption and scattering coefficients for this second phantom set are within the expected ranges for biological tissues. Also, similar to the previous study, the phantoms exhibited the expected trends where absorption and scattering coefficients each increase with increasing concentrations of nigrosin and TiO₂, respectively. As

expected, the concentration of the scattering values, at a constant TiO_2 concentration of 0.05 g / phantom, remains consistent at approximately 1.40, 1.20, and 1.00 at 471 nm, 526 nm, and 621 nm, respectively. Similarly, the absorption values, for constant nigrosin of 0.25 ml / phantom, remain consistent at approximately 0.11, 0.14, and 0.16 at 471 nm, 526 nm, and 621 nm, respectively. Other expected behaviors which were observed were that longer wavelengths resulted in increased absorption and decreased scattering. These factors all lead to two conclusions; first, the process to create stable tissue simulating phantoms is consistent and efficient, and second, that varying proportions of nigrosin and TiO_2 compounds allows flexibility and precision in generating phantoms with quite specific optical properties.

CHAPTER 4: SYSTEM PRECISION & ACCURACY

4.1 SYSTEM CHARACTERIZATION

4.1.1 SYSTEM SENSITIVITY

The sensitivity of the MI system is a key factor in evaluating the dynamic range within which it can accurately operate. The overall sensitivity is primarily a function of the illumination source intensity and the camera's response (which incorporates both the sensor's quantum efficiency and the transmission of the imaging lens). To evaluate the system sensitivity, homogenous grayscale image patches, ranging from 0 to 255 gray levels (black to white) with a 5 gray level step size, were digitally generated and projected onto a white reflective surface. The camera was used to capture the reflected light and measure the gray level being projected. Figure 19 shows the measured relationship between the projected gray levels to the image intensity recorded by the camera. As observed from the graph, projected gray levels below 50 and above 225 are truncated at 25 and 190 gray levels on the sensor. Thus images at reflected intensity levels below 50 and above 225 are not accurately captured. This effect can potentially reduce the imaging dynamic range and consequently limit the operational range of optical properties which can be measured with the system.

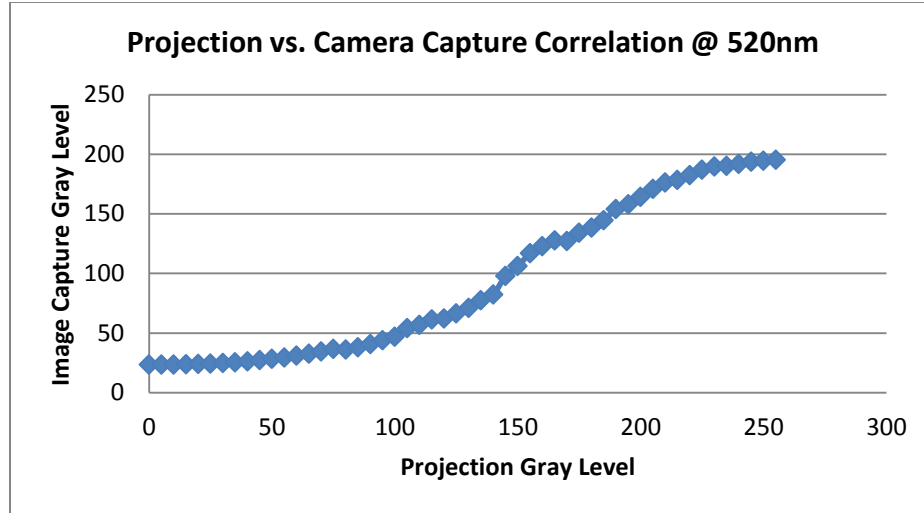


Figure 19: Prototype MI system sensitivity: Grayscale digital projection level vs image captured level

4.1.2 PRECISION AND REPRODUCIBILITY

To measure the inter- and intra-measurement precision and reproducibility of the system, a large homogenous phantom (described in Section 2.2) was imaged (a) repeatedly at the same spatial location, and (b) at different spatial locations using the MI system at a wavelength of 520nm (Figure 20). The diffuse reflectance measured at each frequency ($R_d(f)$) was compared across multiple image repetitions to determine the stability of the system. Figure 20 shows the locations where the two sets of measurements were obtained on a homogenous phantom.

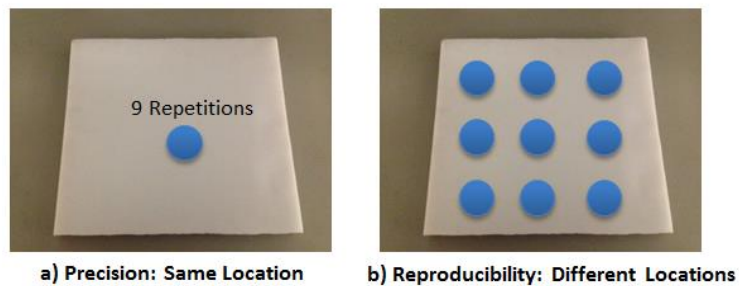


Figure 20: Precision & reproducibility measurement locations

Precision was determined by repeatedly imaging the same spatial location nine times and comparing the diffuse reflectance curves and optical properties calculated from each run. *Reproducibility* was determined by imaging nine different spatial locations on the phantom in a single imaging run, and comparing the diffuse reflectance curves and optical properties calculated at these locations.

Figure 21 shows the diffuse reflectance measurements for the nine repetition measurements for both precision and reproducibility characterization. In both cases, all nine diffuse reflectance curves overlapped each other with a correlation of greater than 0.999. The phantom's optical properties calculated by averaging each set of 9 measurements repetitions were $\mu_a = 0.017 \pm 0.0003 \text{ mm}^{-1}$ and $\mu'_s = 1.54 \pm 0.01 \text{ mm}^{-1}$. The values measured for this phantom by independent FDPM measurement (Figure 13) were $\mu_a = 0.016 \text{ mm}^{-1}$ and $\mu'_s = 1.55 \text{ mm}^{-1}$. The standard deviation of the repeated measurements was less than 1% of the mean in each case, indicating that the system is both highly precise and reproducible.

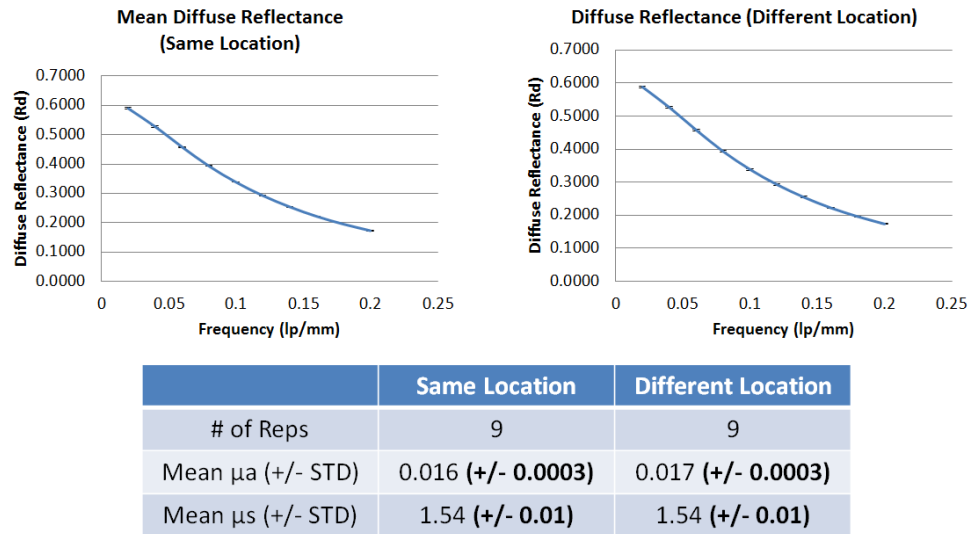


Figure 21: R_d measurements at the same and different locations on a homogeneous phantom

4.2 VARYING PHANTOMS EXPERIMENT

4.2.1 VARYING ABSORPTION / FIXED SCATTERING

As described in the previous chapter, five phantoms with varying nigrosin concentration and a fixed TiO_2 concentration (Phantom set “A”: A1-A5) were created to evaluate the accuracy of the MI system across a range of absorption levels. Each phantom was measured at wavelengths of 470nm, 520nm and 620nm and optical properties calculated. Table 5 shows the absorption (μ_a) and scattering (μ'_s) coefficients obtained for phantoms A1 – A5. Since the phantoms were homogenous, averaging of pixels across the FOV was used to estimate single values for μ_a and μ'_s for each phantom at each wavelength. Increasing nigrosin concentration from phantoms A1 to A5 resulted in an increase in the measured absorption coefficient for all wavelengths (down the columns of Table 5). Further, for any specific nigrosin concentration, the measured absorption coefficient increased with longer wavelengths (across the rows of Table 5). With a fixed TiO_2 concentration, the scattering coefficient is expected to remain constant for all wavelengths across all phantoms. The results in Table 5 show a slight increase in scattering as the nigrosin concentration increases. This behavior was observed for all wavelengths.

Table 5 Prototype System Measurements			Wavelengths [nm]					
			470		520		620	
Phantom	Nigrosin [ml]	TiO ₂ [g]	μ_a	μ'_s	μ_a	μ'_s	μ_a	μ'_s
A1	0.025	0.05	0.006	1.56	0.007	1.30	0.009	0.99
A2	0.075	0.05	0.006	1.59	0.008	1.31	0.010	1.01
A3	0.250	0.05	0.014	1.62	0.017	1.34	0.020	1.04
A4	0.625	0.05	0.034	1.68	0.040	1.43	0.044	1.10
A5	1.665	0.05	0.076	1.88	0.089	1.58	0.090	1.22

Table 5: Phantom set “A”: optical properties measured on the prototype MI system using least-squares fitting to diffuse reflectance at 10 spatial frequencies.

Figures 22 and 23 compare the measured optical properties for the varying absorption / fixed scatter phantoms (set “A”) obtained with the prototype MI system, against the reference system. Since the reference system operates with a specific set of wavelengths, comparison to the prototype system was performed by selecting the closest available wavelengths (471nm, 526nm, and 621nm) in the reference system. As Figure 22 shows, the measured absorption coefficients increase on both systems with increasing nigrosin, although for the highest concentrations of nigrosin (> 1.5ml), the prototype MI system underestimated μ_a at all wavelengths. The scattering coefficient measured using the reference system remained constant for all phantoms at each wavelength, whereas these values increased slightly with increasing nigrosin with the prototype system. Since the “A” set of phantoms had a constant TiO₂ concentration of 0.05g / 55 ml silicone, the scattering coefficients were expected to be consistent, as was observed in measurements with the reference system. This suggested that the phantoms were created appropriately and the cause of the discrepancy lies within the prototype MI system. Figure 23 shows a direct comparison of the optical property measurement between the prototype (y-axis)

and reference (x-axis) MI systems. The dotted lines indicate the relationship for two perfectly correlated systems. For μ_a , the two systems correlate extremely well at all wavelengths, for $\mu_a < 0.05 \text{ mm}^{-1}$. At higher absorption levels, agreement between the systems decreases, with the prototype system appearing to underestimate μ_a . When comparing the calculated μ'_s values for the two systems, a good correlation was observed for the majority of phantoms, except the one with the highest concentration of nigrosin. It can also be observed from the plots that the deviation between the two systems increases at shorter wavelengths (i.e. 471nm and 520nm), which are associated with higher scattering values.

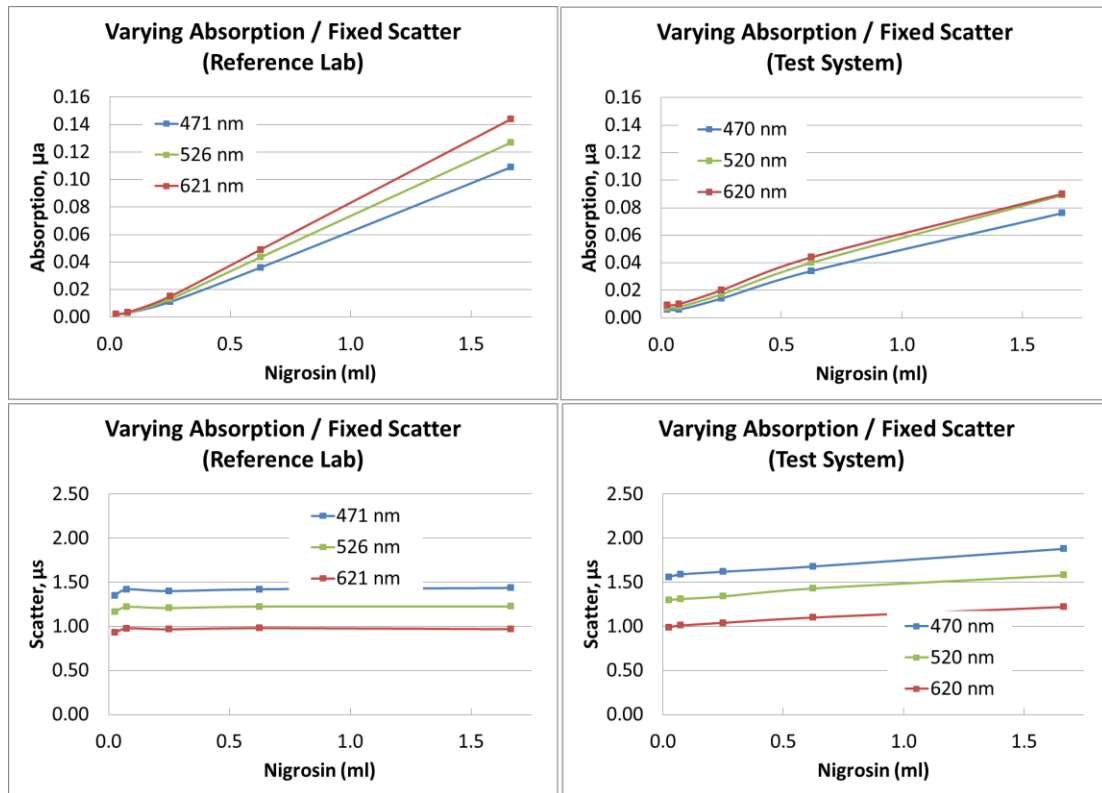


Figure 22: Varying absorption / fixed scattering phantoms: optical properties vs. nigrosin content for reference and test systems

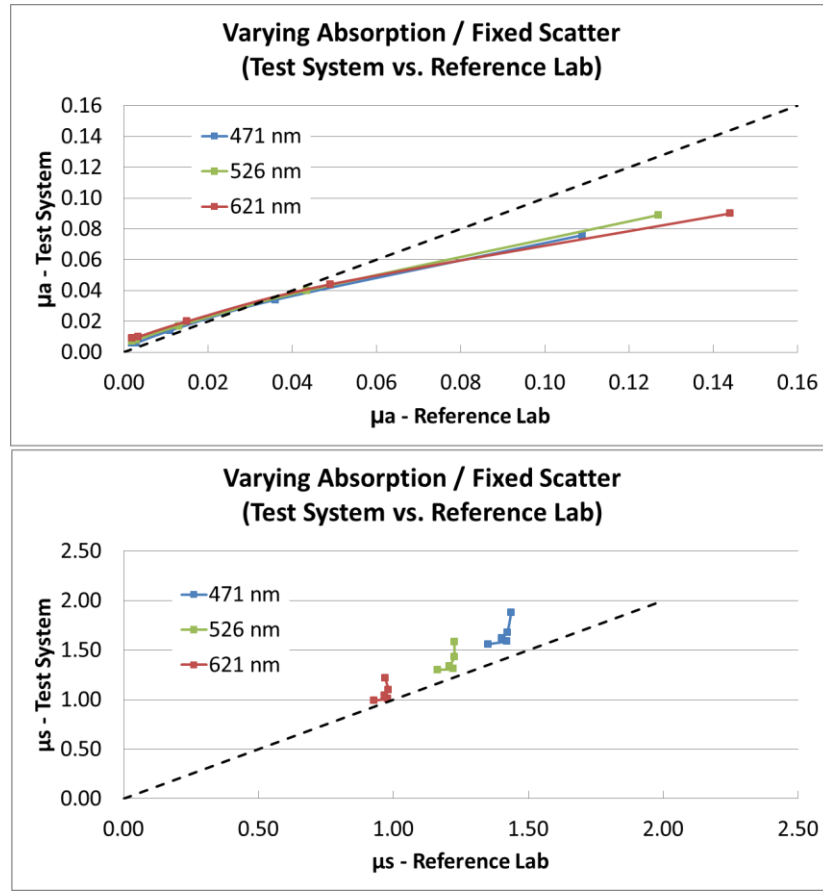


Figure 23: Varying absorption / fixed scattering phantoms: Relationships between reference and test systems for μ_a and μ'_s calculations.

4.2.2 VARYING SCATTERING / FIXED ABSORPTION

Six phantoms with varying TiO_2 concentration and fixed nigrosin concentration (Phantom set “B”: B1-B5, plus A3) were used to evaluate the accuracy of the MI system across a range of scattering levels. Each phantom was measured in the prototype MI system at wavelengths of 470nm, 520nm and 620nm. Table 6 shows the absorption (μ_a) and reduced scattering (μ'_s) coefficients obtained for the six phantoms. Values reported again represent the optical properties derived from averaging diffuse reflectance values across all pixels within the FOV. Increasing TiO_2 concentration (phantoms B1 \rightarrow B5)

resulted in an increase in measured scattering coefficient for all wavelengths. For any specific TiO_2 concentration, scattering decreased with longer wavelengths. With a fixed nigrosin concentration, the absorption coefficient is expected to remain consistent for all wavelengths across all phantoms. The results in Table 6 show consistent μ_a values for $\text{TiO}_2 > 0.05\text{g} / 55 \text{ ml silicone}$. Below this concentration (phantoms B1 and B2), calculated μ_a values significantly increased at all wavelengths.

Table 6 Prototype System Measurements			Wavelengths [nm]					
			471		526		621	
Phantom	Nigrosin [ml]	TiO_2 [g]	μ_a	μ'_s	μ_a	μ'_s	μ_a	μ'_s
B1	0.25	0.0250	0.035	1.28	0.037	1.03	0.042	0.86
B2	0.25	0.0375	0.021	1.36	0.025	1.12	0.029	0.89
A3	0.25	0.0500	0.014	1.62	0.018	1.34	0.020	1.04
B3	0.25	0.0625	0.013	1.74	0.016	1.43	0.019	1.10
B4	0.25	0.0750	0.012	1.90	0.016	1.57	0.018	1.18
B5	0.25	0.0875	0.009	2.11	0.013	1.76	0.016	1.30

Table 6: Phantom set “B”: optical properties measured on the prototype MI system using least-squares fitting to diffuse reflectance at 10 spatial frequencies.

Figures 24 and 25 compare the phantom optical properties measured by the prototype system to those obtained with the reference system. As Figure 24 shows, the measured μ'_s increases on both systems with increasing TiO_2 , although for high ($> 0.08\text{g}$) and low ($< 0.04\text{g}$) concentrations of TiO_2 , the test MI system underestimates and overestimates μ'_s , respectively. Further, the value of μ_a measured using the reference system remains fairly constant for all phantoms at the three wavelengths, whereas absorption is slightly higher for low concentration of TiO_2 with the test system. Since

these phantoms had a constant nigrosin concentration of 0.25ml / 55 ml silicone, the measured μ_a is expected to be consistent, which is observed with the reference system. Similar to the varying absorption results, this suggests the cause of the discrepancy lies within the prototype MI system, since all phantoms showed the expected trends when measured with the reference system. Figure 25 shows a direct comparison of the optical property measurements at each wavelength, between the prototype (y-axis) and reference (x-axis) MI systems. The diagonal dotted line indicates the theoretical relationship between two systems in perfect agreement. For the scattering prediction, the correlation plots for all the wavelengths are slightly rotated along the diagonal, indicating a decrease in correlation for low and high μ_a . For determination of μ_a , the systems generally correlated well for most of the phantoms except the ones with the lowest TiO_2 concentrations. Although TiO_2 should have no direct effect of the absorption properties of the phantom, the lowest values of TiO_2 (<0.05g) seem to falsely induce additional absorption of the phantom in the test system. As the figure shows, the effect is similar for all wavelengths.

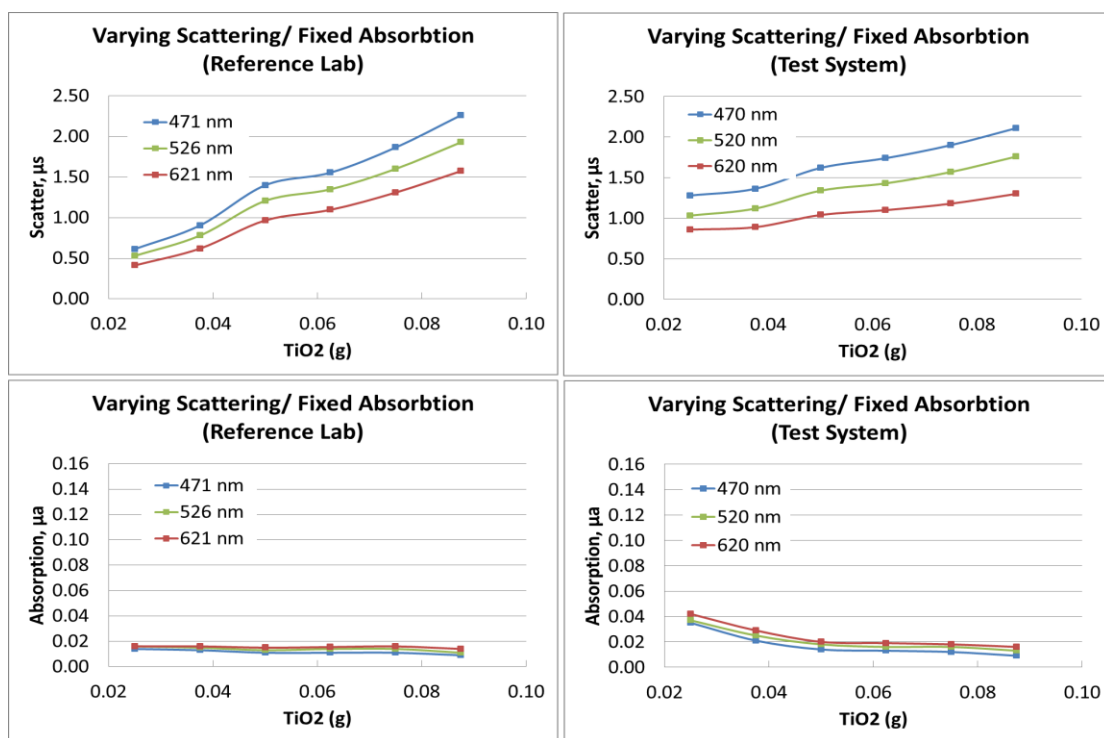


Figure 24: Varying scattering / fixed absorption phantoms: optical properties vs. TiO_2 content for reference and test systems.

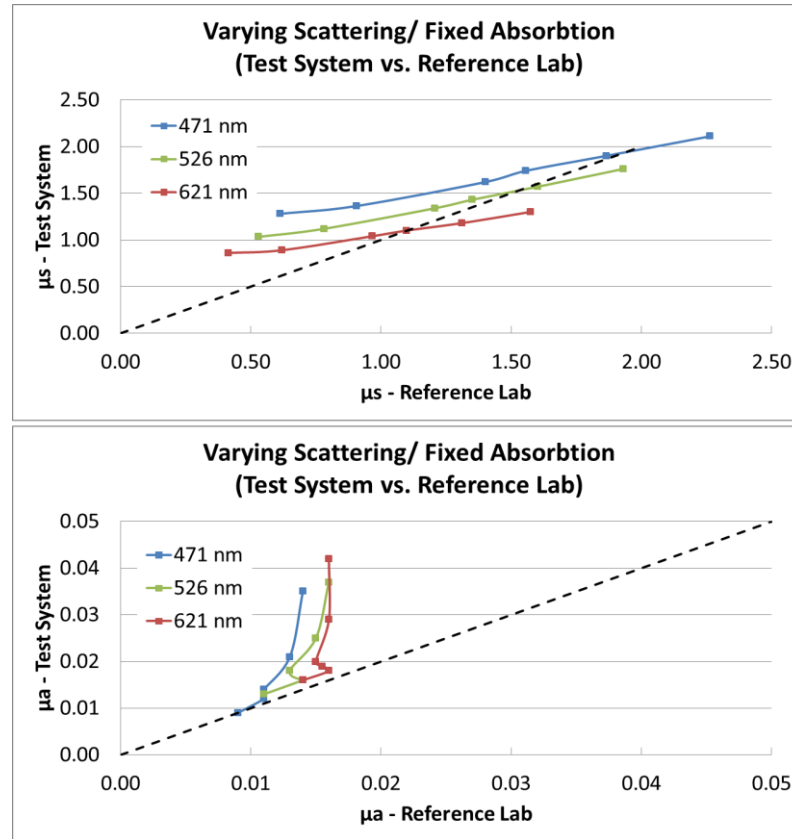


Figure 25: Varying Absorption/Fixed Scattering phantoms: Relationships between reference and test systems for μ_a and μ'_s calculations.

4.2.3 OVERALL ACCURACY TO REFERENCE SYSTEM

The accuracy evaluation of the test system using the varying absorption and scattering phantoms revealed several key pieces of information regarding its performance and limitations. Firstly, both sets of phantoms demonstrated that the test system behaved similarly across the different wavelengths in terms of under- and overestimation in comparison to the reference system. Alternatively, it was observed that scattering coefficient measurements performed at 620nm have slightly better accuracy compared to the other wavelengths. The scattering correlation plot in Figure 23 (bottom) shows the clusters for each wavelength, with the measurements at 620nm being closest to the

diagonal dotted line (perfect correlation) as compared to the other wavelengths. The scattering correlation plots from Figure 25 (top) show that μ'_s measurements with the prototype MI system at each wavelength exhibit a similar trend in comparison to the reference system, although the measurements at 620nm are closer to the ideal correlation line. Both scattering correlation plots from the varying absorption and scattering studies demonstrate a trend of increasing accuracy with higher excitation wavelengths.

Figure 26 shows all measurements of μ_a and μ'_s with the prototype MI system and the reference system, pooled across the three wavelengths in order to obtain an estimate of the overall system accuracy for optical property measurement (Table 7). For μ_a calculation, a range where the prototype MI system agrees well with the reference system was identified as spanning approximately $0.09 < \mu_a < 0.049 \text{ mm}^{-1}$ (indicated with dotted green lines). Within this range, the prototype MI system exhibited an average error of 16% relative to the reference system. For μ'_s calculation, a range with good agreement with the reference system was determined to span approximately $0.93 < \mu'_s < 2.23 \text{ mm}^{-1}$ (indicated with dotted green lines), where the prototype MI system exhibited an average error of 10% relative to the reference system. Outside these ranges of optical properties, the error on the values determined by the prototype system increased significantly, with low μ_a and μ'_s values having errors as high as 150-350%.

Overall Accuracy (FIT vs. Reference)	Absorption(μ_a)	Scattering (μ_s)
Average Error (%)	16%	10%
Range	0.09 - 0.049 mm^{-1}	0.93 - 2.23 mm^{-1}

Table 7: Overall accuracy between proposed MI and reference system using Method 1

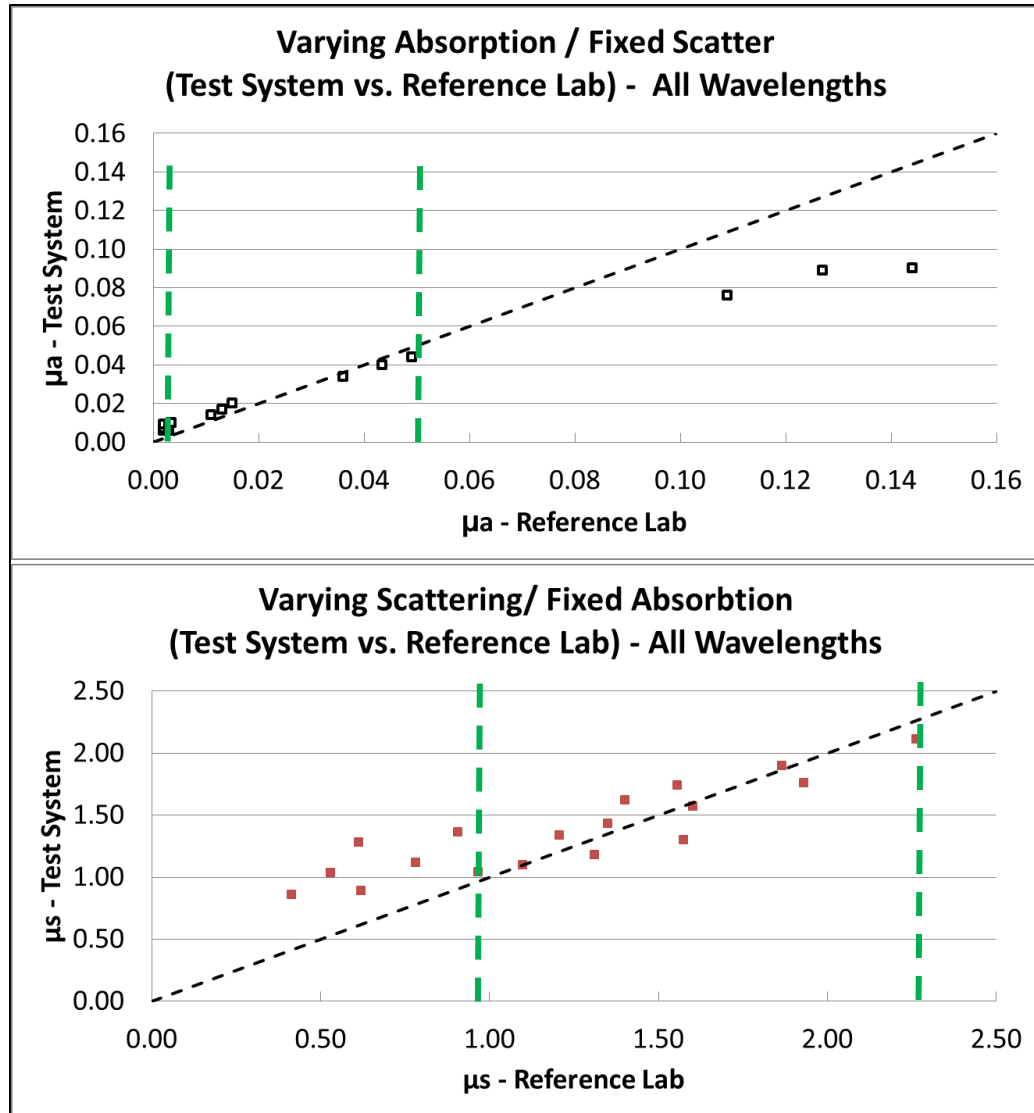


Figure 26: Overall correlations in phantom optical properties measurements between reference and test systems (for all wavelengths combined)

4.2.4 ROOT CAUSE ANALYSIS OF DIFFERENCES

While the prototype MI system developed here demonstrated reasonable agreement with a reference MI system for a limited range of optical properties (Table 7), additional analysis was required to understand the source of the discrepancies outside these ranges, and identify opportunities for improvements to the prototype system. A

recurring trend observed with all optical property measurements was that the largest errors were associated with the highest or lowest concentrations of TiO_2 or nigrosin. This observation suggests that the test phantoms may generate diffuse reflectance (R_d) values outside the dynamic range of the system sensitivity (Figure 19), resulting in inaccurate measurements on phantoms that are too strongly absorbing, or too strongly scattering. To assess this behavior, the diffuse reflectance versus spatial frequency data ($R_d(f)$) was evaluated for both sets of phantoms (set “A” and set “B”). According to the underlying diffusion-based model for $R_d(f)$, (Cuccia et. al. 2009, eq. 10), higher spatial frequencies are expected to result in lower diffuse reflectance, resulting in a darker appearing images. Since it is these measured $R_d(f)$ plots which ultimately determine the optical properties of the sample, comparing the raw diffuse reflectance data measured with the prototype system to values predicted by the diffusion-based model could provide further insight into the effect(s) of operating with a limited system dynamic range.

Figure 27 shows the diffuse reflectance curves measured with the prototype MI system (blue) with the theoretically predicted curves (red) for the phantoms with varying μ_a and fixed μ'_s . Increasing μ_a (phantoms A1 to A5) results in darker appearing phantoms. Phantoms A1 and A2, with the lowest μ_a show a measured $R_d(f)$ curve which is lower than the theoretical curve at low f , and higher than the theoretical curve at high f . Phantom A3 demonstrates a measured $R_d(f)$ curve which agrees well with theory at low f , but remains higher than the theoretical curve at high f . As μ_a increases further in phantoms A4 and A5, the measured $R_d(f)$ curves are uniformly higher than theoretical predictions across all frequencies, although the trend of both curves remains similar.

Figure 28 shows a similar trend for phantoms with fixed μ_a and varying μ'_s (phantom set “B”). In this phantom set, the sample transitions from a dark to light appearance as the TiO_2 concentration increases (B1 \rightarrow B5). B1 and B2, the two lowest scattering phantoms, again show a significant offset between the measured and theoretically predicted $R_d(f)$ curves, with the measured curve being consistently higher than predicted. Phantoms B3 and B4, with higher TiO_2 concentration, show curves with good agreement between measured and predicted R_d . Phantom B5, with the highest μ'_s , begins to display an offset between the two curves, although now with the measured curve lower than predicted by theory. Therefore, for both sets of phantoms (“A” and “B”), the darker phantoms (higher μ_a or lower μ'_s) show measured $R_d(f)$ curves consistently higher than theory, while the lighter phantoms (lower μ_a or higher μ'_s) show measured curves being consistently lower than theory.

These trends demonstrated by both sets of phantoms indicate that the prototype MI system is unable to accurately measure diffuse reflectance (R_d) values above and below certain levels. High and low R_d values may arise from measuring samples with high concentrations of absorbing or scattering components, or when imaging with low or high spatial frequencies. The result of inaccurately measuring the $R_d(f)$ relationship is a significant error in subsequent calculation of optical properties. This observation largely points to the limited dynamic range of the system, as shown earlier in Figure 19, being responsible for inaccurate measurements at low and high R_d . This is potentially due to a combined effect of the illumination source and the camera, which should ideally be upgraded to a higher performance model in subsequent MI systems.

Figure 27: Measured and theoretical diffuse reflectance plots for phantom set A1-A5.

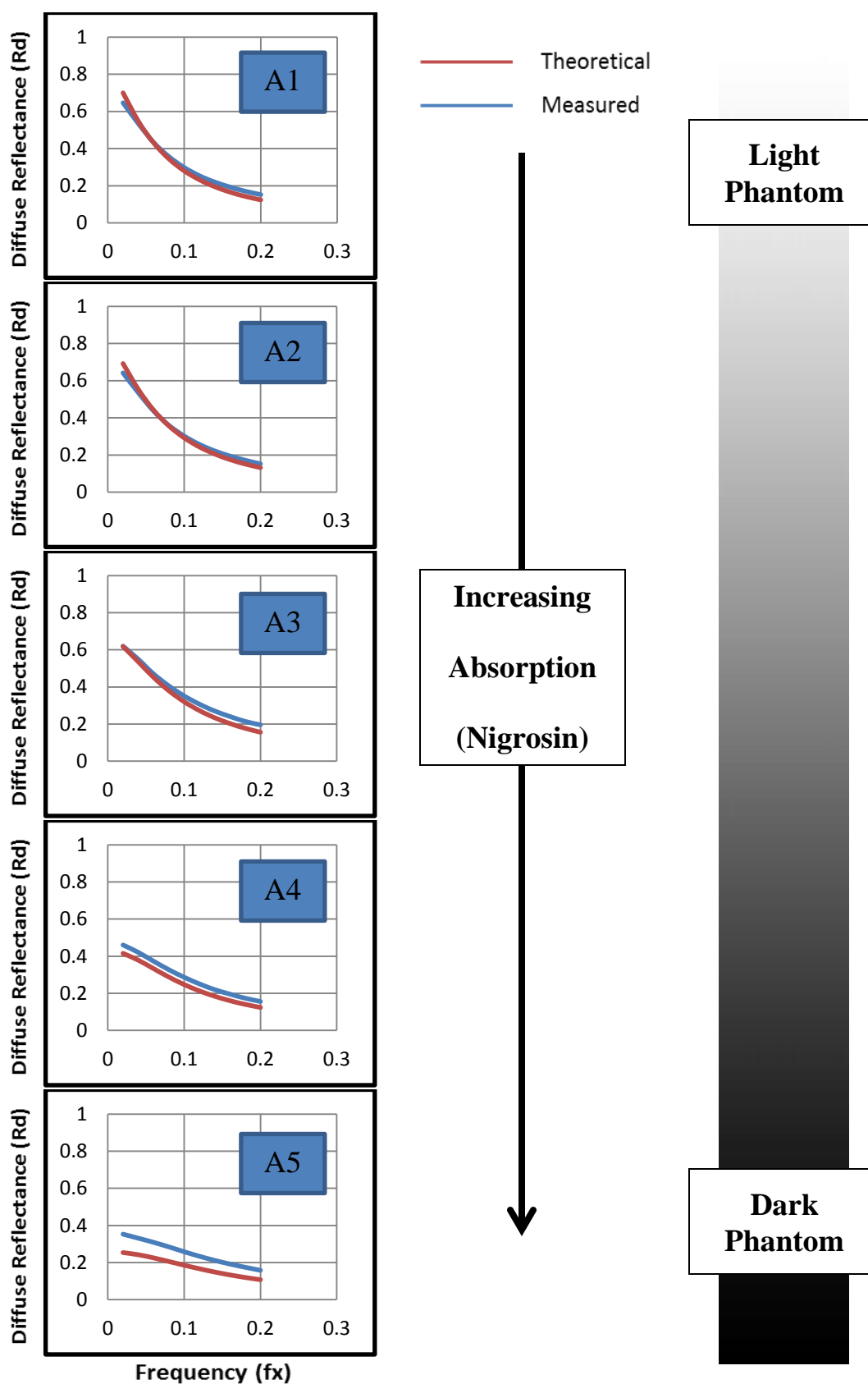
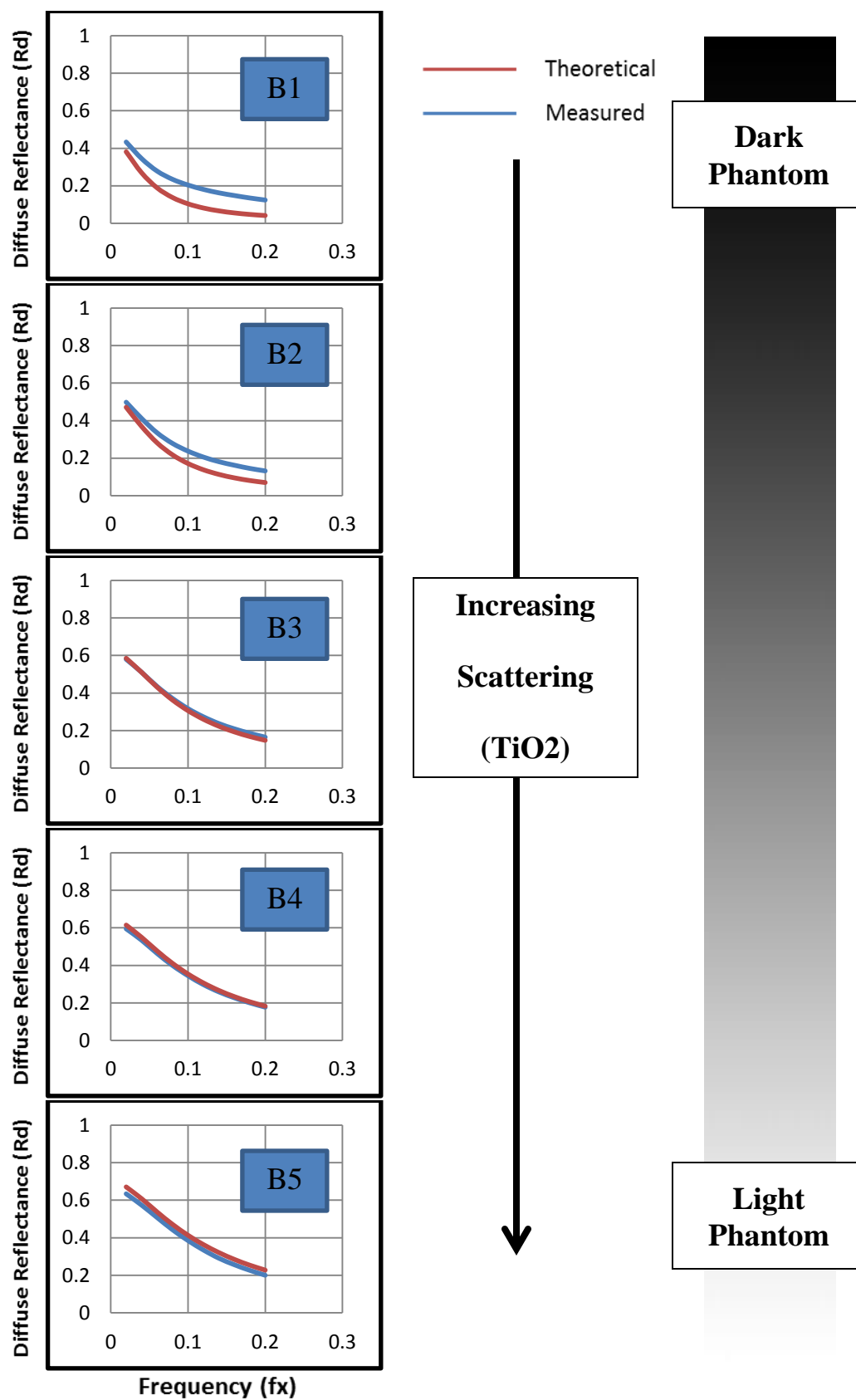


Figure 28: Measured and theoretical diffuse reflectance plots for phantom set B1-B5.



4.3 2-FREQUENCY LUT - METHOD EVALUATION

The data described so far allowed the accuracy of the prototype MI system to be quantified when using least-squares fitting of an analytical diffusion-based model for $R_d(f, \mu_a, \mu'_s)$ to the experimentally measured $R_d(f)$ from multiple phantoms, with μ_a and μ'_s as fitting parameters. Although this model fitting approach substantiates the MI principle, in practice, its utility is reduced to homogenous samples, where measured $R_d(f)$ values can be averaged across all pixels in the FOV before proceeding with μ_a and μ'_s calculation. Fitting a single $R_d(f, \mu_a, \mu'_s)$ curve to ten measured $R_d(f)$ values takes approximately 2.5 seconds. Since MI provides a 10-frequency $R_d(f)$ relationship for each pixel in an image, applying this model fitting method to each pixel individually within a 3.5mm x 2mm sample region, could potentially take 30 days per sample! Therefore, the model fitting approach is only feasible in homogenous samples where the $R_d(f)$ values measured at all pixels can be averaged at each frequency (f) to obtain a single $R_d(f)$ relationship for the entire sample.

To achieve utility of MI in clinical applications, where the majority of samples requiring imaging are heterogeneous and real-time measurement may be desirable, a more efficient method for determining optical properties from diffuse reflectance measurements was recently proposed (Erickson, Mazhar et al. 2010). This approach is based on generating a theoretical lookup table (LUT) of predicted R_d values which would result from specific combinations of μ_a and μ'_s , when illuminated with each of only two spatial frequencies (f_1 and f_2) (Figure 3). As described in Chapter 1, the diffuse reflectance model (eq. 1) is a function of illuminating spatial frequency (f), absorption (μ_a) and scattering (μ'_s) coefficients (at any given wavelength). Since diffuse reflectance

(R_d) can be measured for any specific spatial frequency (f), to solve the system of equations with two unknown (μ_a and μ'_s) requires only two unique equations. Based on this concept, a LUT of R_d values can be generated for all combinations of absorption and scattering coefficients at two illumination spatial frequencies. Then, by imaging a sample *at those specific frequencies only*, the measured diffuse reflectance values ($R_d(f_1)$ and $R_d(f_2)$), can be easily and quickly mapped to a unique pair of μ_a and μ'_s values via the LUT. This method enables calculation of optical properties at each pixel in an entire FOV by only using R_d measurements at two spatial frequencies, making the modulated imaging concept more practical for laboratory and clinical applications.

The LUT method was incorporated in the prototype MI system and its accuracy for determining μ_a and μ'_s values was compared to the 10-frequency model fitting method. Based on inspection of the raw diffuse reflectance curves for the phantoms used in the study (Figure 29), spatial frequencies at $f_1 = 0.02 \text{ mm}^{-1}$ and $f_2 = 0.10 \text{ mm}^{-1}$ were selected with the goal of providing adequate discrimination of optical properties. These plots demonstrate that samples with different μ_a can be distinguished by their diffuse reflectance at *low* spatial frequencies; above $f \approx 0.10 \text{ mm}^{-1}$, there is little contrast in the R_d values for phantoms A1 – A5 (with varying absorption). Similarly, the lower plot in Figure 29 demonstrates that samples with different μ'_s can best be distinguished by their diffuse reflectance at spatial frequencies in the range $0.05 < f < 0.10 \text{ mm}^{-1}$. At high spatial frequencies, the R_d values converge to similar values, regardless of scattering coefficient. Therefore a LUT was generated using $f_1 = 0.02 \text{ mm}^{-1}$ and $f_2 = 0.10 \text{ mm}^{-1}$ in the (forward) diffusion-based model.

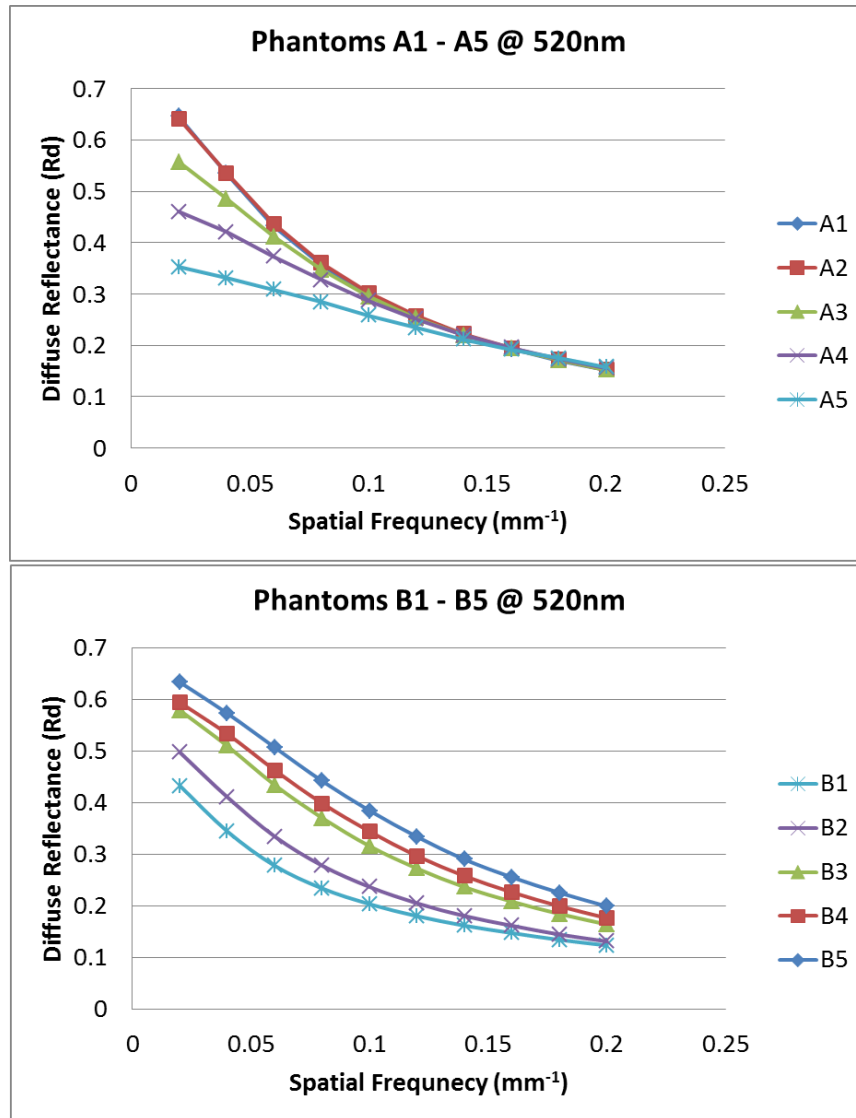


Figure 29: Diffuse reflectance (R_d) vs. spatial frequency for phantom set “A” (top) and phantom set “B” (bottom)

To perform a direct comparison of methods, data obtained for all phantoms with the model fitting method was used to re-calculate each phantom’s optical properties from only the R_d values at the two spatial frequencies employed by the LUT. Figure 30 shows the correlation between the two methods in estimating μ_a (top plot) and μ'_s (bottom plot). As observed from the plots, the data points predominantly lie along the diagonal, indicating that the methods are in good agreement. The additional error resulting from

use of the LUT method is approximately 2% and 4% for μ_a and μ'_s values, respectively. However, the reduction in computational time is almost 80%.

Figure 31 demonstrates an example of using the LUT method to image a composite FOV containing phantoms with different optical properties and to generate μ_a and μ'_s values at each pixel of the image. As observed with these maps, the user can quickly and easily visualize and quantify the optical properties of a heterogeneous sample, demonstrating the potential of MI in medical imaging applications.

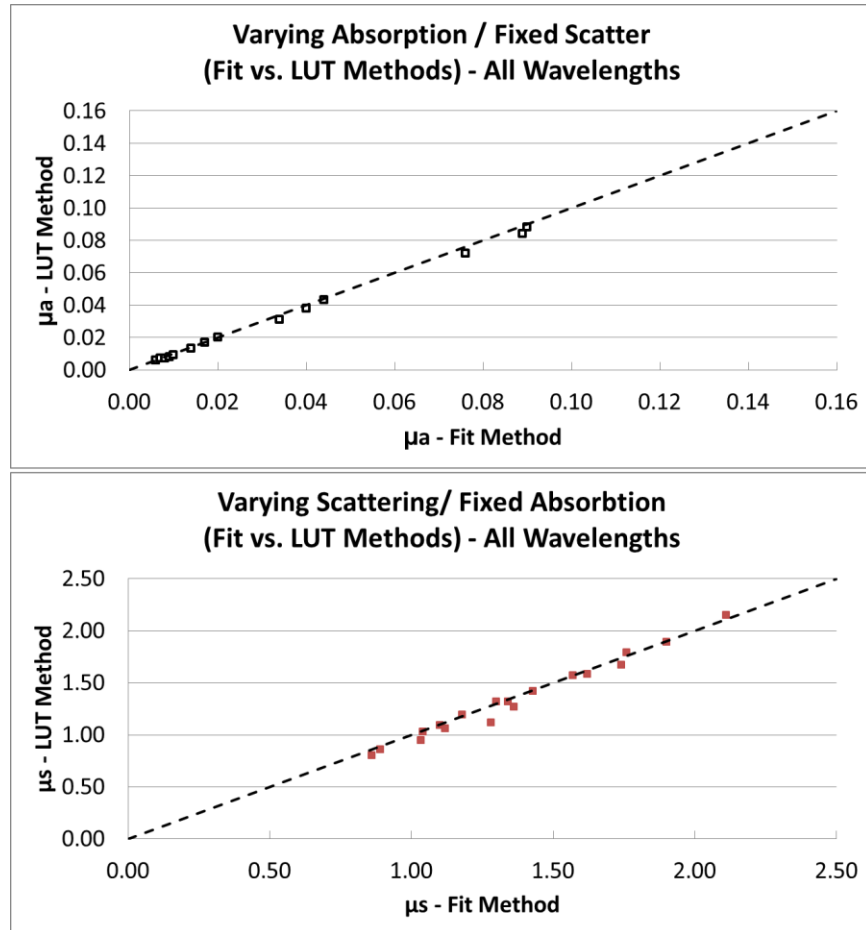


Figure 30: Relationships between optical property measurements generated by least-squares fitting (FIT) and lookup table (LUT) methods.

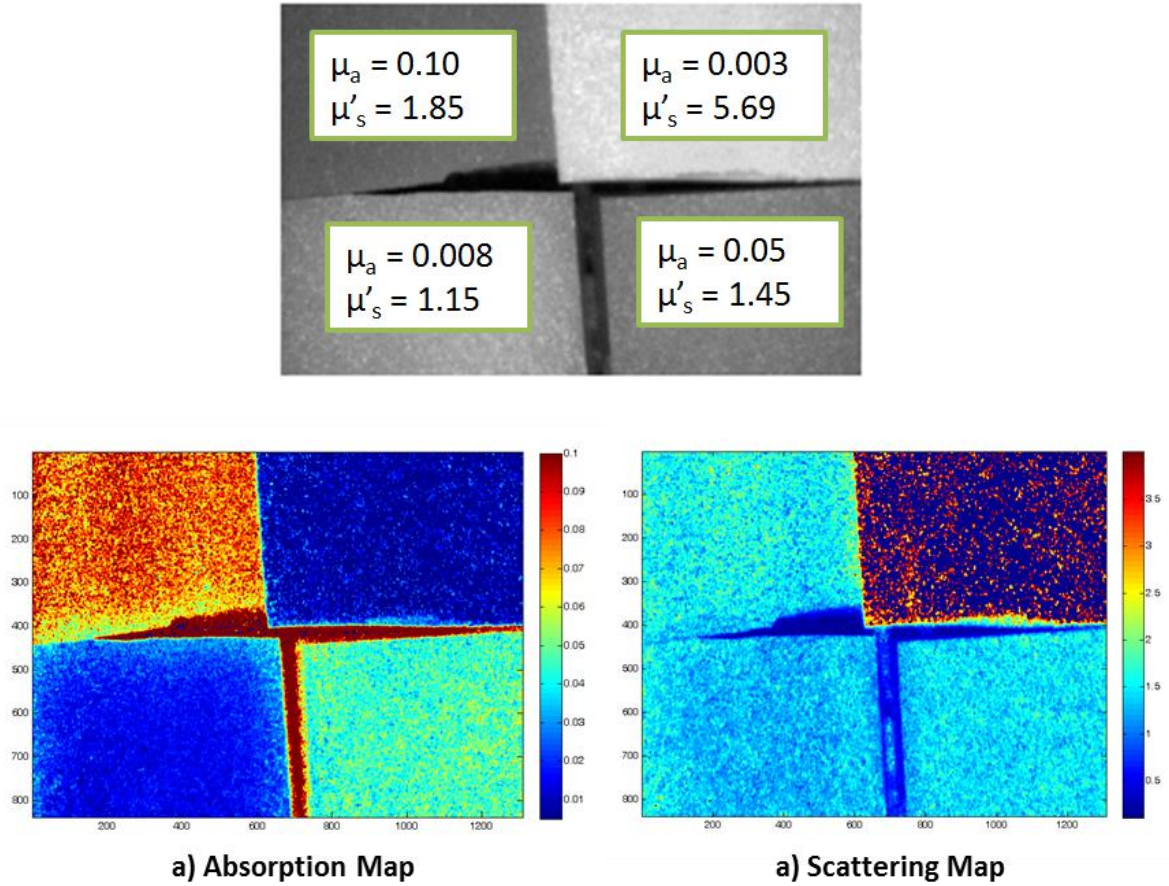


Figure 31: Example of optical property mapping of a phantom composite: Four phantoms with different absorption and scattering properties were imaged in a single FOV, with values from the reference MI system overlaid on each (top). Optical property maps were generated using the LUT method (bottom).

4.4 ABSORPTION SPECTRUM PREDICTION

So far, the bulk of the study has demonstrated the development and characterization of a MI system to obtain optical properties at three specific wavelengths (470nm, 520nm, 620nm), chosen on the basis of the projector's output intensity (Figure 8). In theory, the method could be applied across a wide range of wavelengths, ultimately resulting in measurement of continuous absorption and scattering spectra, $\mu_a(\lambda)$ and $\mu'_s(\lambda)$. These spectra can directly provide additional insight into the sample

being imaged, or can be analyzed further to quantify the concentrations of tissue chromophores (e.g. oxy-/deoxy- hemoglobin, lipids, and water) which contribute to the overall spectra (Gioux, Mazhar et al. 2011). However, applying MI at many different wavelengths will lead to a decrease in the imaging speed, potentially defeating the purpose of the technology. Therefore, a novel approach is proposed in which performing MI at only four wavelengths can rapidly generate continuous optical property spectra.

To test the approach, a phantom with its complete absorption and scattering spectrum established using FDPM at UC Irvine was imaged using the prototype MI system at four wavelengths; 470nm, 520nm, 620nm, and 790nm. For each wavelength, the diffuse reflectance $R_d(\lambda)$ was obtained at only two spatial frequencies ($f_1 = 0.10 \text{ mm}^{-1}$ and $f_2 = 0.20 \text{ mm}^{-1}$), with measurement results shown in Table 8. The diffuse reflectance versus wavelength relationships (at f_1 and f_2) were each fit to an exponential equation (Figure 32) to obtain predicted diffuse reflectance curves spanning the entire visible spectrum. These predicted diffuse reflectance spectra are then applied back to the LUT based on the two measurement spatial frequencies, to obtain the absorption spectrum across all visible wavelengths. Figure 33 shows the predicted absorption spectrum using the proposed “four wavelength” method to the actual spectrum measured across all wavelengths by FDPM, showing good agreement.

Wavelength	Rd @ (0.1 lp/mm)	Rd @ (0.2 lp/mm)
470	0.41	0.22
520	0.34	0.18
620	0.26	0.12
790	0.19	0.08

Table 8: Diffuse reflectance (R_d) measured at four different wavelengths and two spatial frequencies

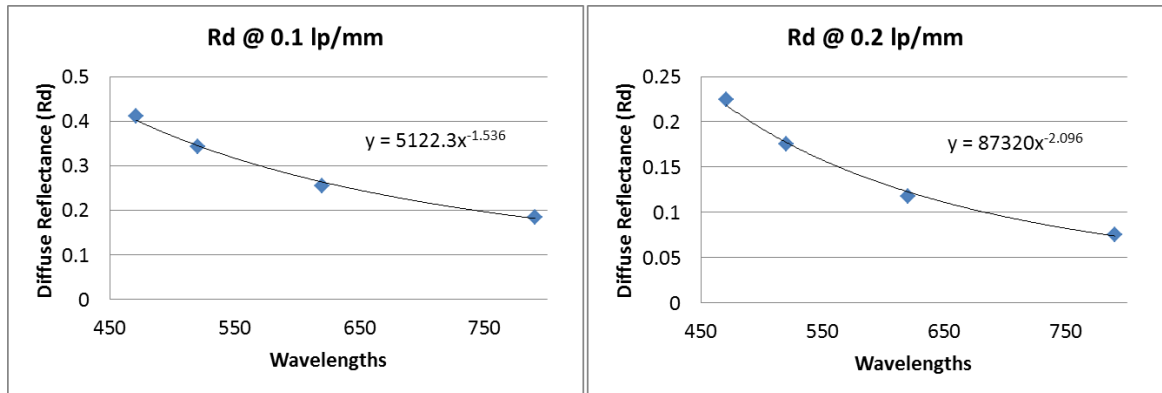


Figure 32: Diffuse reflectance (R_d) measured at 4 wavelengths (470nm, 520nm, 620nm, 790nm) and fit to an exponential function for spatial frequencies of 0.10 lp/mm and 0.20 lp/mm.

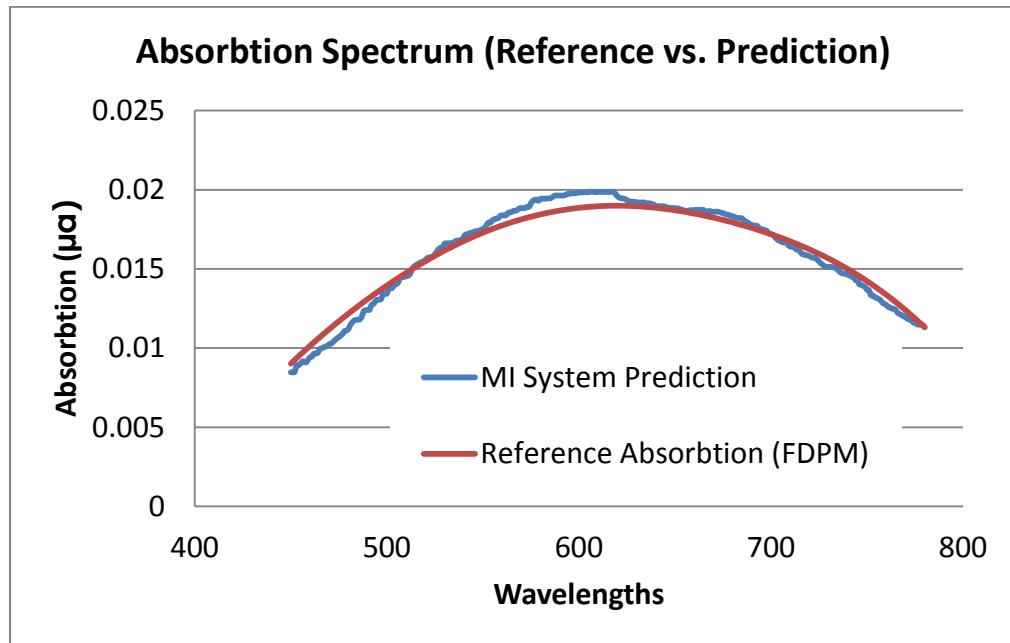


Figure 33: Comparison between the actual absorption spectrum measured using continuous FDPM and the MI system prediction using only four wavelengths with extrapolation.

CHAPTER 5: DISCUSSION

5.1 DISCUSSION OF RESULTS

Spatial frequency domain imaging (SFDI) or Modulated imaging (MI) was introduced in 2005 (Cuccia, Bevilacqua et al. 2005) and has since been investigated for use in several clinical applications, primarily for quantitative, non-contact monitoring of tissue oxygenation via measurement of oxy- and deoxyhemoglobin concentrations. The start-up company *Modulated Imaging Inc.* (www.modulatedimaging.com) will supply MI systems to researchers on a per-order basis, with pricing in the region of \$60-70k per unit. The aim of this thesis was to develop a low-cost MI platform using off-the-shelf hardware and open-source software, which would be sufficiently flexible to enable future customization and optimization for specific applications. This work required selection and integration of discrete hardware components and development of a software application to both control the hardware elements, and perform post-processing of captured image data. The prototype MI system was configured to measure optical properties at three different wavelengths; 470nm, 520nm, and 620nm, and its performance was compared to a system from the *Modulated Imaging* company to assess measurement accuracy.

Any newly developed imaging system requires complete characterization to establish measurement precision and reproducibility. To achieve this, a large, homogenous phantom was imaged repeatedly at the same physical location, and then at different locations on the phantom surface. As shown through diffuse reflectance versus

spatial frequency ($R_d(f)$) curves and subsequent optical property estimation, the prototype system exhibits high stability, with an overall correlation greater than 0.999 in diffuse reflectance curves and total variability below 2% in calculating optical properties. This initial assessment is a key factor for any imaging setup, as it confirms that the components such as the camera and illumination source are stable, and any measurement performed of the system is reliable.

The next step in characterizing system performance was comparison of its accuracy relative to a reference standard. Tissue simulating phantoms were created by combining nigrosin and TiO_2 in a silicone matrix, allowing variation of absorption and scattering properties, respectively. An initial set of phantoms covering a wide range of nigrosin and TiO_2 concentrations were developed and measured using the reference MI system to obtain approximate relationships between the concentrations of nigrosin and TiO_2 and the resulting μ_a and μ'_s . Based on the data from this initial set of phantoms, a second “test” set of phantoms was fabricated with absorption and scattering coefficients spread over suitable biologically relevant ranges for validating the accuracy of the prototype MI system.

Similar to studies performed by other groups (Cuccia, Bevilacqua et al. 2009), two sets of “test” phantoms were developed; set “A” with varying absorption and constant scattering, and set “B” with varying scattering and constant absorption. Both sets of phantoms were initially measured on the reference system, with absorption and scattering coefficients obtained at the three reference system wavelengths (471nm 526nm and 621nm) which match closest to the prototype MI system developed here. With phantom set “A”, the reference system measured absorption coefficients which linearly

increased with increasing concentration of nigrosin, while the measured scattering coefficients remained constant. For phantom set “B”, a similar increase in scattering coefficients was measured with increasing concentration of TiO_2 whereas the absorption coefficients remained constant. When measured with the prototype MI system, similar trends were observed for the phantom sets with varying concentrations of nigrosin and TiO_2 , although for the fixed components, deviation in the corresponding optical properties were observed in phantoms at the low and/or high concentration ends of the varying components. This behavior was easily observed when the measurements from the prototype and reference systems were plotted against each other. The regions where disagreements between systems were observed were consistent for all three wavelengths, although for majority of the comparisons, the 620nm wavelength had slightly smaller deviations compared to the other wavelengths (520nm and 470nm). Pooling the measurements for all measured phantoms across the three wavelengths clearly showed a high degree of correlation between systems for a limited range of μ_a and μ'_s . The range within which the prototype system correlated highly with the reference system was approximately $0.090 - 0.049 \text{ mm}^{-1}$ for μ_a and $0.93 - 2.23 \text{ mm}^{-1}$ for μ'_s . The average error in optical property determination for the prototype system was approximately 16% and 10% for μ_a and μ'_s , respectively.

The degree of correlation between prototype and reference systems at high and low scattering and absorption values suggested the cause to be associated with the dynamic range and sensitivity of the system. Earlier, the sensitivity of the system had been evaluated by projecting a range of digitally generated grayscale patches onto a uniform target and measuring the reflectance with the camera. Truncation of measured

intensity values at approximately 30 and 190 at the low and high ends of the 8-bit grayscale range (0-255), indicated initially that the system may not perform well for samples with very low and very high diffuse reflectance. Such samples would be those with high absorbance / low scatter and low absorbance / high scatter, respectively. To determine whether the diffuse reflectance measurements on the phantoms were outside the dynamic range of the prototype system, measured R_d versus f curves were compared to theoretically predicted curves, for each of the phantoms. As described in the previous chapter, the diffuse reflectance values measured in the prototype system were divergent from the theoretical values for the darkest and lightest phantoms (those with lowest and highest reflectance, respectively), and also for imaging at high and low spatial frequencies (also corresponding to low and high reflectance, respectively). Comparison of the experimental and theoretical plots clearly showed that the diffuse reflectance values measured in the prototype system were lower than the theoretical value for light phantoms and low spatial frequencies, and higher than the theoretical value for dark phantoms and high frequencies. Thus, some of the phantoms measured at specific illumination spatial frequencies resulted in very low or very high diffuse reflectance intensities that were outside the dynamic range of the system.

The limited dynamic range of the system is a combined characteristic of both the illuminating projector and the camera sensor. Although this limitation is present at all wavelengths, the slightly better agreement between measurement and theory at the 620nm wavelength can possibly be attributed to the increased sensitivity of the camera at the longer wavelength end of the spectrum, as shown in the quantum efficiency curves for the camera (Figure 34).

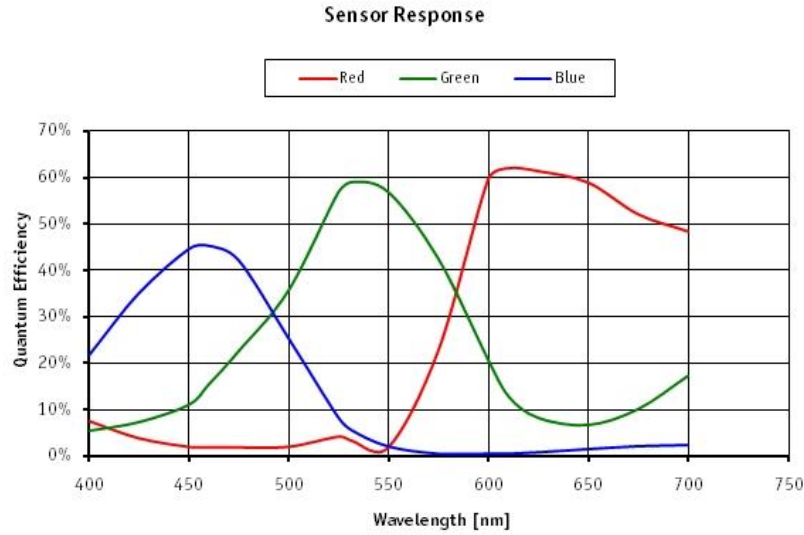


Figure 34: Camera sensor response curves (from Point Grey Research)

An important modification to the MI processing method was implemented in the prototype system, to make it more applicable to real-time medical imaging applications. As explained earlier, while the optical properties of the object being imaged can be determined by a least squares fit of a diffusion-based analytical model to the measured $R_d(f)$ data, in practice this approach is only feasible for use in homogenous samples where R_d values can be reduced to a single value at each spatial frequency (f) by averaging over all spatial pixels. This limitation is due to the significant time it takes to perform the fitting process for a set of diffuse reflectance values across ten spatial frequencies (2.5 seconds per R_d curve). Since imaging is typically performed over a 2-D space with diffuse reflectance measured at each pixel in an image, it would be advantageous to calculate optical properties at each pixel, generating 2-D absorption and scattering maps of the object. Since the majority of medical imaging applications involve heterogeneous samples, completing pixel-by-pixel optical property calculations in a reasonable timeframe is a key requirement for adoption by potential end users. The group who

initially developed the MI technology later proposed a lookup table (LUT) method that was able to address this issue (Erickson, Mazhar et al. 2010). As described earlier, the analytical model for diffuse reflectance R_d is a function of illumination spatial frequency (f), μ_a , and μ'_s . This forward model was used to generate predictions for R_d over a range of μ_a , and μ'_s values, at each of only two distinct spatial frequencies, f_1 and f_2 . The resulting map then allowed measured R_d values at f_1 and f_2 to be mapped to a unique pair of μ_a , and μ'_s values. Thus, solving the inverse problem only requires imaging at two spatial frequencies (instead of the ten used for the fitting method). Implementation of the LUT method resulted in measurements with high correlation to the fitting method, with an error of only 2% and 4% for μ_a and μ'_s values, respectively. The LUT method reduced the acquisition and processing time by 80% because only two spatial frequencies were required, and allowed optical property determination at each image pixel within a few seconds. Use of the LUT approach to generate spatially-resolved optical property maps was tested by imaging four unique phantoms with varying μ_a and μ'_s . The method was highly accurate in distinguishing the phantoms from each other and accurately calculating the optical properties.

5.2 PROPOSED FUTURE WORK

Modulated imaging (MI) has emerged as a potentially useful technique for performing non-invasive and rapid quantification of tissue optical properties. The work completed in this thesis has created and validated a low-cost MI platform that will enable users to easily customize parameters to optimize the technology for specific future applications. Based on the findings of this work, the most important next step with the

current MI system is to upgrade the illumination and sensor components to increase the dynamic range of the system. As shown earlier, outside of a specific range of optical properties, the system generates μ_a and μ'_s values which can differ widely from those generated by a reference system. The primary recommended upgrade would be a change in the illumination source. The current projector used is an off-the-shelf, low-grade DLP “Pico” projector with a relatively weak built-in broadband light source (7 lumens). An upgrade to the illumination source can be achieved by acquiring one of the higher brightness DLP projectors which have since arrived on the market. “Pico” (hand-held) and “pocket” sized projectors are now available with several hundreds of lumens output brightness (e.g., the Optoma ML550 with 500 lumens in a 1.5"x4.1"x4.2", 0.9 lb unit costs under \$500). Alternatively, a customizable projector (e.g. Texas Instruments *Light Commander*) can be easily coupled with an external, high powered, LED for even higher intensity illumination.

After expanding the dynamic range of the MI system to accurately measure optical properties across desired wider range, the next step would be to incorporate excitation bandpass filters specific to the target application. As mentioned earlier, the original motivation behind building the MI system was to perform non-invasive quantification of lipid concentration in liver. Thus, illumination wavelengths which provide the highest separation between absorption and scattering spectra of lipids should be used, in order to increase the accuracy of decomposing the measured μ_a spectrum into contributions from individual chromophores. The technique demonstrated in the previous chapter, uses just four wavelengths to accurately predict a full absorption spectrum. The ultimate goal of this technology would be to quantify the absorption and

scattering coefficients at discrete measurement wavelengths, and then use pre-determined basis spectra for the primary chromophores at those wavelengths to determine the lipid concentration by principal component analysis. This could potentially serve as a technique to analyze livers during the de-fatting process and determine if the liver has reached the state acceptable for transplantation, without the need to extract biopsies and wait for lab results.

5.3 SUMMARY AND CONCLUSION

In conclusion, a fully functional modulated imaging (MI) system was developed from the ground up, enabling rapid and accurate quantification of sample optical properties. The system was characterized for stability and the dynamic range was determined within which it can function accurately. The MI system was developed in such a way that it would provide future users with complete flexibility of modifying individual components such as the camera, light source, and projection patterns, with only a simple re-calibration required after each modification. Further, the user is also provided with the ability to easily change the bandpass filters to achieve any desired excitation wavelength. These are key features to have access to for optimizing the technology for specific applications.

Liver transplantation has faced challenges for several decades in keeping up with the current patient demand. The increasing obesity trend in the current population further complicates the available donor pool and causes livers to be ineligible for transplantation due to excess lipid concentration. A great deal of research is being performed in several different areas in order to increase the available donor pool (Izamis, Calhoun et al. 2013),

including the concept of defatting fatty livers to make them eligible for transplantation use. Though the process has proven to have potential, it faces other challenges that limit the use of the technology (Nativ, Maguire et al. 2012). The MI system developed in this thesis may provide a unique approach to rapidly quantify the lipid concentration without extracting biopsies, addressing both the issue of turnaround time for determining if the liver is ready and keeping the liver organ intact throughout the regeneration process.

CHAPTER 6: REFERENCES

- Abookasis, D., et al. (2009). "Imaging cortical absorption, scattering, and hemodynamic response during ischemic stroke using spatially modulated near-infrared illumination." Journal of Biomedical Optics **14**(2): 024033-024033-024039.
- Auger, J.-C., et al. (2009). "Theoretical study of the scattering efficiency of rutile titanium dioxide pigments as a function of their spatial dispersion." Journal of Coatings Technology and Research **6**(1): 89-97.
- Bassi, A., et al. (2008). "Spatial shift of spatially modulated light projected on turbid media." Journal of the Optical Society of America A **25**(11): 2833-2839.
- Berthiaume, F., et al. (2009). "Steatosis Reversibly Increases Hepatocyte Sensitivity to Hypoxia-Reoxygenation Injury." The Journal of surgical research **152**(1): 54-60.
- Bessemers, M., et al. (2007). "Preservation of steatotic livers: A comparison between cold storage and machine perfusion preservation." Liver Transplantation **13**(4): 497-504.
- Canelo, R., et al. (1999). Is a fatty liver dangerous for transplantation? Transplantation proceedings, Elsevier.
- Chowdhury, S. and J. Izatt (2013). "Structured illumination quantitative phase microscopy for enhanced resolution amplitude and phase imaging." Biomedical Optics Express **4**(10): 1795-1805.
- Cuccia, D. J. (2012). Spatial Frequency Domain Imaging (SFDI): a technology overview and validation of an LED-based clinic-friendly device.
- Cuccia, D. J., et al. (2009). "Quantitation and mapping of tissue optical properties using modulated imaging." Journal of Biomedical Optics **14**(2): 024012-024012-024013.
- Cuccia, D. J., et al. (2005). "Modulated imaging: quantitative analysis and tomography of turbid media in the spatial-frequency domain." Optics Letters **30**(11): 1354-1356.
- Erickson, T. A., et al. (2010). "Lookup-table method for imaging optical properties with structured illumination beyond the diffusion theory regime." Journal of Biomedical Optics **15**(3): 036013-036013-036019.
- Gioux, S., et al. (2011). "First-in-human pilot study of a spatial frequency domain oxygenation imaging system." Journal of Biomedical Optics **16**(8): 086015-086015-086010.

Guarrera, J. V., et al. (2011). "Hypothermic Machine Preservation Attenuates Ischemia/Reperfusion Markers After Liver Transplantation: Preliminary Results." The Journal of surgical research **167**(2): e365-e373.

Henry, S. D., et al. (2012). "Hypothermic Machine Preservation Reduces Molecular Markers of Ischemia/Reperfusion Injury in Human Liver Transplantation." American Journal of Transplantation **12**(9): 2477-2486.

Izamis, M.-L., et al. (2013). "Simple Machine Perfusion Significantly Enhances Hepatocyte Yields of Ischemic and Fresh Rat Livers." Cell Medicine **4**(3): 109-123.

Jamieson, R. W., et al. (2011). "Hepatic Steatosis and Normothermic Perfusion—Preliminary Experiments in a Porcine Model." Transplantation **92**(3): 289-295
210.1097/TP.1090b1013e318223d318817.

Konecky, S. D., et al. (2009). "Quantitative optical tomography of sub-surface heterogeneities using spatially modulated structured light." Optics Express **17**(17): 14780-14790.

Mazhar, A., et al. (2010). "Wavelength optimization for rapid chromophore mapping using spatial frequency domain imaging." Journal of Biomedical Optics **15**(6): 061716-061716-061719.

Mazhar, A., et al. (2012). "Spatial frequency domain imaging of port wine stain biochemical composition in response to laser therapy: A pilot study." Lasers in Surgery and Medicine **44**(8): 611-621.

Mazhar, A., et al. (2012). Implementation of an LED-based clinical spatial frequency domain imaging system.

Merion, R. M., et al. (2005). "The Survival Benefit of Liver Transplantation." American Journal of Transplantation **5**(2): 307-313.

Mokuno, Y., et al. (2002). Reconditioning of fatty livers for transplantation increased survival of recipients in a rat model. Engineering in Medicine and Biology, 2002. 24th Annual Conference and the Annual Fall Meeting of the Biomedical Engineering Society EMBS/BMES Conference, 2002. Proceedings of the Second Joint.

Nagrath, D., et al. (2009). "Metabolic preconditioning of donor organs: Defatting fatty livers by normothermic perfusion ex vivo." Metabolic Engineering **11**(4-5): 274-283.

Nativ, N. I., et al. (2012). "Liver Defatting: An Alternative Approach to Enable Steatotic Liver Transplantation." American Journal of Transplantation **12**(12): 3176-3183.

O'Sullivan, T. D., et al. (2012). "Diffuse optical imaging using spatially and temporally modulated light." Journal of Biomedical Optics **17**(7): 0713111-07131114.

Ogden, C. L., et al. (2012). Prevalence of obesity in the United States, 2009-2010, US Department of Health and Human Services, Centers for Disease Control and Prevention, National Center for Health Statistics.

Pifferi, A., et al. (2005). "Determination of visible near-IR absorption coefficients of mammalian fat using time- and spatially resolved diffuse reflectance and transmission spectroscopy." Journal of Biomedical Optics **10**(5): 054004-054004-054006.

Pogue, B. W. and M. S. Patterson (2006). "Review of tissue simulating phantoms for optical spectroscopy, imaging and dosimetry." Journal of Biomedical Optics **11**(4): 041102-041102-041116.

Ponticorvo, A., et al. (2013). "Quantitative assessment of partial vascular occlusions in a swine pedicle flap model using spatial frequency domain imaging." Biomedical Optics Express **4**(2): 298-306.

Presser, C. (2012). "Absorption coefficient measurements of particle-laden filters using laser heating: Validation with nigrosin." Journal of Quantitative Spectroscopy and Radiative Transfer **113**(8): 607-623.

Sokal, E., et al. (2008). "End-stage liver disease and liver transplant: current situation and key issues." Journal of pediatric gastroenterology and nutrition **47**(2): 239-246.

Weber, J. R., et al. (2009). "Noncontact imaging of absorption and scattering in layered tissue using spatially modulated structured light." Journal of Applied Physics **105**(10): -.

Weber, J. R., et al. (2006). Modulated Imaging in Layered Media. Engineering in Medicine and Biology Society, 2006. EMBS '06. 28th Annual International Conference of the IEEE.